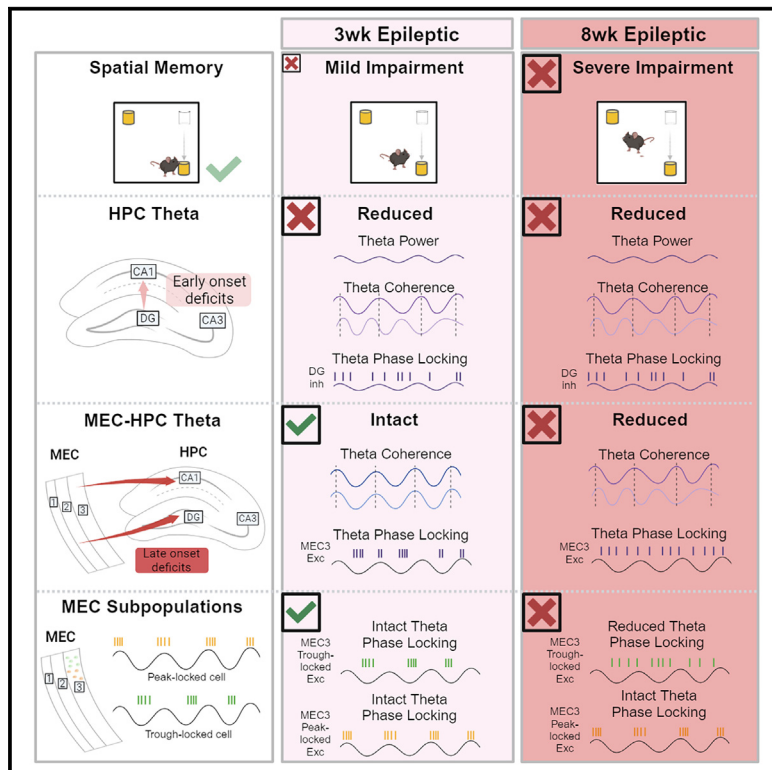


## Distinct changes to hippocampal and medial entorhinal circuits emerge across the progression of cognitive deficits in epilepsy

### Graphical abstract



### Authors

Yu Feng, Keziah S. Diego, Zhe Dong, ..., Nadia N. Khan, Denise J. Cai, Tristan Shuman

### Correspondence

tristan.shuman@mssm.edu

### In brief

Feng et al. demonstrate that memory deficits in temporal lobe epilepsy involve multiple discrete mechanisms with distinct time courses. In epileptic mice, early-onset memory deficits are associated with disrupted hippocampal synchronization, while more severe, late-onset impairments are associated with disrupted synchrony of medial entorhinal cortex circuits.

### Highlights

- Epileptic mice have progressive memory impairments dissociable from seizures
- Early memory impairment is minor and associated with hippocampal desynchronization
- More severe memory deficits are associated with reduced MEC-hippocampal synchrony
- MEC3 neurons active at the trough of theta are uniquely impaired in epileptic mice



## Article

# Distinct changes to hippocampal and medial entorhinal circuits emerge across the progression of cognitive deficits in epilepsy

Yu Feng,<sup>1</sup> Keziah S. Diego,<sup>1</sup> Zhe Dong,<sup>1</sup> Zoé Christenson Wick,<sup>1</sup> Lucia Page-Harley,<sup>1</sup> Veronica Page-Harley,<sup>1</sup> Julia Schnipper,<sup>1</sup> Sophia I. Lamsifer,<sup>1</sup> Zachary T. Pennington,<sup>1</sup> Lauren M. Vetere,<sup>1</sup> Paul A. Philipsberg,<sup>1</sup> Ivan Soler,<sup>1</sup> Albert Jurkowski,<sup>1</sup> Christin J. Rosado,<sup>1</sup> Nadia N. Khan,<sup>1</sup> Denise J. Cai,<sup>1</sup> and Tristan Shuman<sup>1,2,\*</sup>

<sup>1</sup>Nash Family Department of Neuroscience, The Friedman Brain Institute, Icahn School of Medicine at Mount Sinai, New York, NY, USA

<sup>2</sup>Lead contact

\*Correspondence: [tristan.shuman@mssm.edu](mailto:tristan.shuman@mssm.edu)

<https://doi.org/10.1016/j.celrep.2024.115131>

## SUMMARY

Temporal lobe epilepsy (TLE) causes pervasive and progressive memory impairments, yet the specific circuit changes that drive these deficits remain unclear. To investigate how hippocampal-entorhinal dysfunction contributes to progressive memory deficits in epilepsy, we performed simultaneous *in vivo* electrophysiology in the hippocampus (HPC) and medial entorhinal cortex (MEC) of control and epileptic mice 3 or 8 weeks after pilocarpine-induced status epilepticus (Pilo-SE). We found that HPC synchronization deficits (including reduced theta power, coherence, and altered interneuron spike timing) emerged within 3 weeks of Pilo-SE, aligning with early-onset, relatively subtle memory deficits. In contrast, abnormal synchronization within the MEC and between HPC and MEC emerged later, by 8 weeks after Pilo-SE, when spatial memory impairment was more severe. Furthermore, a distinct subpopulation of MEC layer 3 excitatory neurons (active at theta troughs) was specifically impaired in epileptic mice. Together, these findings suggest that hippocampal-entorhinal circuit dysfunction accumulates and shifts as cognitive impairment progresses in TLE.

## INTRODUCTION

Temporal lobe epilepsy (TLE) is the most common form of adult-onset epilepsy<sup>1</sup> and is often associated with cognitive impairment that significantly impacts quality of life.<sup>2–8</sup> Cognitive deficits in epilepsy are generally dissociable from chronic seizures,<sup>9,10</sup> suggesting that these symptoms are driven by separate neural mechanisms, yet no treatments have been developed to directly address cognitive impairment. In both people with TLE and rodent models, there is extensive cell death<sup>11–14</sup> and axonal sprouting<sup>15–18</sup> throughout the temporal lobe that are likely to impair normal function and lead to cognitive deficits. However, the pathological changes in neuroanatomy, gene expression, and behavior each emerge at different time points after an initial epileptogenic insult. Likewise, the symptoms of epilepsy,<sup>19,20</sup> including cognitive impairment,<sup>2–5,21</sup> often progressively worsen over time. These progressive changes in behavior likely reflect the continual emergence of pathological changes to the underlying neural circuits. Therefore, it is critical to understand how circuit dysfunction emerges across the timeline of epileptogenesis in order to link changes in behavior with specific circuit changes and to develop new ways to directly treat cognitive impairment in epilepsy.

Normal cognitive function requires precisely timed neural activity in order to induce plasticity and create stable memory representations.<sup>22</sup> In particular, theta oscillations are strongly

associated with memory processing and are thought to synchronize neural activity within and across brain regions in order to facilitate the formation of stable representations.<sup>23–34</sup> In rodent models of TLE, there is extensive evidence of abnormal hippocampal processing that is likely to contribute to memory impairments. For instance, in chronically epileptic rodents, Cornu Ammonis 1 (CA1) place cells in the hippocampus (HPC) are less precise and less stable than in control animals.<sup>35–38</sup> These changes in spatial coding also coincide with an array of changes in network-wide synchronization throughout the HPC. In particular, epileptic rodents have decreased theta power and coherence in HPC,<sup>35,39–41</sup> as well as altered theta phase precession in CA1<sup>36</sup> and altered theta phase locking of dentate gyrus (DG) inhibitory cells.<sup>35</sup> Together, these findings suggest that the synchronization of theta oscillations and neural spiking are disrupted in epileptic animals. However, it remains unclear how these network changes progress after epileptogenesis and which changes might contribute to the emergence of memory impairments.

While most studies of TLE have focused on the HPC, there are extensive anatomical changes in the medial entorhinal cortex (MEC) in patients<sup>42–46</sup> and in rodent models.<sup>47</sup> The MEC is the primary spatial input into HPC and is critical for spatial navigation and memory,<sup>26,48,49</sup> suggesting that it may have a prominent role in epilepsy-associated cognitive deficits. MEC provides spatial information to HPC through grid,<sup>50</sup> border,<sup>51</sup> head direction,<sup>52</sup>



and speed<sup>53</sup> coding projections from two primary pathways: a direct input from layer 3 (MEC3) to CA1 and an indirect input from layer 2 (MEC2) stellate cells to the DG.<sup>54–56</sup> These spatial inputs converge in the HPC, which creates a conjunctive representation of space and experience. This process relies on the precise timing of MEC inputs to drive plasticity,<sup>57</sup> and thus, a breakdown in synchronization between MEC and HPC may lead to altered spatial coding and memory performance. While one study has found an abnormal phase lag of theta oscillations between the DG and MEC2,<sup>58</sup> no studies have examined the synchronization of theta oscillations and spike timing throughout the HPC and MEC across the time course of epileptogenesis.

We previously found progressive deficits in the stability of CA1 spatial coding in epileptic mice that emerged ~6 weeks after pilocarpine-induced status epilepticus (Pilo-SE).<sup>35</sup> Notably, these changes were dissociable from the emergence of spontaneous seizures and deficits in the precision of CA1 place cells, which had already begun 3 weeks after Pilo-SE. This suggests that there are multiple pathological mechanisms driving distinct epilepsy phenotypes, with early changes producing seizures and decreased CA1 spatial precision and later changes diminishing the stability of CA1 spatial representations. However, it remains unclear how these changes in spatial representations relate to memory impairments and altered synchronization in the hippocampal-entorhinal system.

Here we used simultaneous *in vivo* electrophysiology in the HPC and MEC of awake, behaving mice to determine how these key memory circuits are disrupted during the progression of memory impairments following epileptogenesis. We found distinct changes in synchronization across the hippocampal-entorhinal system that paralleled the worsening of memory deficits from 3 to 8 weeks after Pilo-SE. At the early time point, we found extensive disruptions in the synchronization of hippocampal theta and single unit firing in epileptic mice but only minor spatial memory deficits. By the late time point, when memory impairment was more severe, we found disrupted synchronization within the MEC and between the MEC and HPC. Furthermore, within the MEC, we found that a distinct population of excitatory neurons in MEC3, active near the trough of theta oscillations, was specifically disrupted in epileptic mice. Together, these results suggest that the severity of spatial memory impairments is paralleled by the severity of disruptions in network-wide communication within the MEC and between the MEC and HPC.

## RESULTS

### Spatial memory deficits in epileptic mice progressively worsen from 3 to 8 weeks after Pilo-SE, and this progression cannot be explained by seizures or cell loss in the HPC or MEC

Spatial memory deficits are well established in mouse models of TLE<sup>39,59–62</sup> but are typically examined many weeks after epileptogenesis, preventing examination of the progression of behavioral changes. Therefore, we first set out to establish the time course of spatial memory deficits in the Pilo-SE model of chronic TLE. We previously found that epileptic mice have impaired spatial coding in CA1, with early deficits in spatial precision (i.e., information content) already emerging at 3 weeks after

Pilo-SE and late-onset deficits in spatial stability<sup>35</sup> emerging around 6–8 weeks after Pilo-SE. We therefore performed a novel object location (NOL) task in male control and epileptic mice either 3 or 8 weeks after Pilo-SE (Figure 1A). The NOL task is a well-established measure of spatial memory<sup>63,64</sup> that is dependent on both HPC<sup>65</sup> and MEC.<sup>66</sup> Animals were first exposed to two identical objects in a 1 × 1 ft arena. After a 3-h delay, they were placed back in the same arena with one object moved to a new location. We used two separate training protocols in order to vary the difficulty of the task. In the easier version of this task (labeled “easy”), the training session consisted of three 6-min back-to-back exposures, while the more challenging version (labeled “hard”) consisted of only two 6-min exposures. Spatial memory was assessed by the discrimination index (DI), which represents the preference to investigate the moved object over the unmoved object (Figure 1B, see STAR Methods).

Using the “easy” NOL task, we found progressive memory deficits that emerged between 3 and 8 weeks after Pilo-SE. At 3 weeks after Pilo-SE, both control and epileptic animals showed a preference for the moved object (Figure 1C). However, by 8 weeks after Pilo-SE, the epileptic animals no longer showed a preference for the moved object (Figure 1D). Thus, on this “easy” NOL task, epileptic mice showed progressively worse performance from 3 to 8 weeks after Pilo-SE.

We next increased the difficulty of the NOL task to probe for more subtle changes in memory (Figure 1B). In this “hard” NOL task, control mice showed a preference for the moved object, but epileptic mice at both 3 and 8 weeks after Pilo-SE did not show a preference (Figures 1E and 1F). Importantly, during training, both control and epileptic mice spent an equal amount of time exploring both objects, and raw exploration times during test sessions were consistent with the DI metric (Figure S1). Together, these results indicate that spatial memory deficits in epileptic mice are relatively subtle at the 3-week time point and progressively worsen between 3 and 8 weeks after Pilo-SE.

Neuronal cell death is well established in chronic epilepsy,<sup>67–74</sup> and it is possible that the progressive changes in memory performance could reflect ongoing cell death. To characterize the time course of neurodegeneration and cell loss, we performed FluoroJade C (FJC, a marker of degenerating neurons) staining<sup>75</sup> and neuronal nuclei (NeuN) immunohistochemistry (a neuronal marker)<sup>76</sup> in the HPC and MEC at 2 days, 3 weeks, or 8 weeks after Pilo-SE. We found extensive FJC expression 2 days after Pilo-SE in all areas examined, but minimal staining 3 weeks or 8 weeks after Pilo-SE (Figures S2A–S2H), indicating that any neurodegeneration primarily occurs within 2 days after Pilo-SE. This was further confirmed by NeuN immunohistochemistry, which showed significantly reduced NeuN expression in the dentate hilus (Hil) and the ventral portion of MEC3 beginning 2 days after Pilo-SE and remained at a similar level across the 3-week and 8-week time points (Figures S2I–S2M). We did not find significantly reduced NeuN staining in the dorsal portion of MEC2 or MEC3 in epileptic mice, suggesting that the high levels of FJC staining (Figures S2A–S2H) do not necessarily lead to permanent cell loss in these areas (Figures S2I–S2M). Together, these data indicate that most neuronal cell loss in the HPC and MEC of epileptic mice occurs within 2 days of Pilo-SE and is therefore unlikely to directly drive the progression of memory

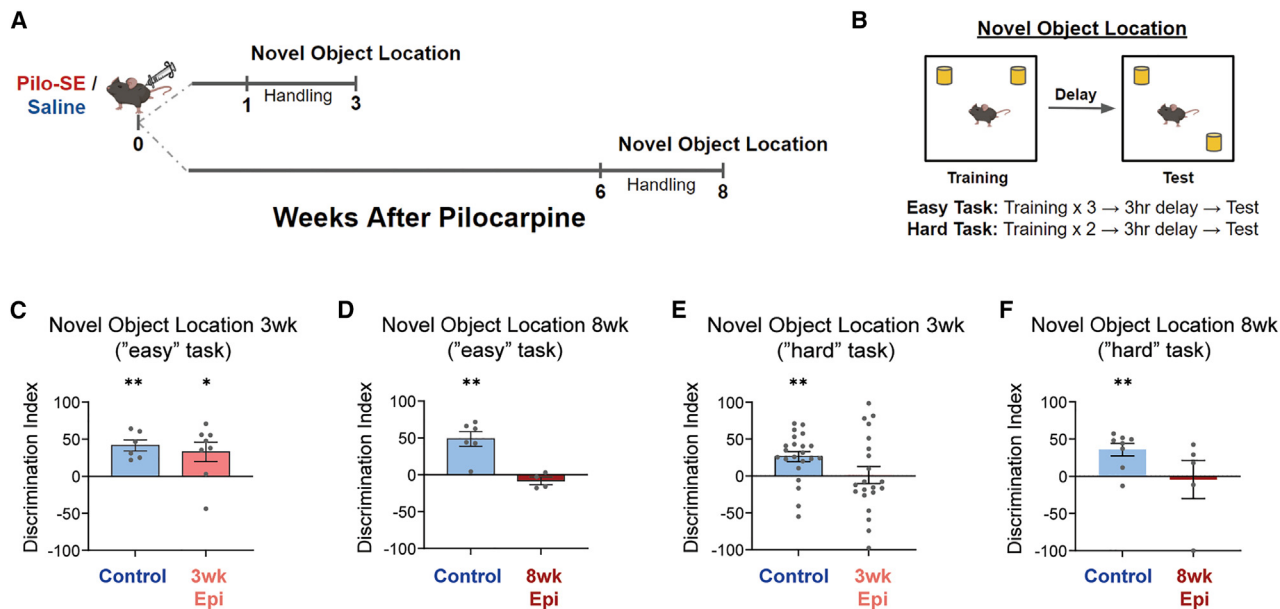


**Figure 1. Early-onset and progressive spatial memory deficits after Pilo-SE**

(A) Timeline of behavioral testing for the novel object location (NOL) task.

(B) NOL training was performed using an “easy” (three 6-min training trials) or “hard” (two 6-min training trials) version of the task. Testing occurred 3 h after the final training sessions.

(C) On the “easy” version of the NOL task, both control and 3-week epileptic (3-week Epi) groups demonstrated a significant preference for the moved object.

(D) At 8 weeks after Pilo-SE, the control mice showed a preference for the moved object on the “easy” NOL task, while the 8-week epileptic (8-week Epi) mice showed no preference.

(E and F) On the “hard” NOL task, neither the 3-week (E) nor the 8-week (F) epileptic mice showed a preference to investigate the moved object, while age-matched control mice showed a significant preference to investigate the moved object.

Error bars represent SEM \* $p < 0.05$ , \*\* $p < 0.01$ . See also Figure S1.

deficits between 3 and 8 weeks after Pilo-SE (Figures 1C and 1D).

We also found that progressive memory deficits (Figures 1C and 1D) are dissociable from seizure frequency and interictal epileptiform discharge (IED) frequency as we observed no differences in seizure or IED frequency between epileptic mice at 3 or 8 weeks after Pilo-SE (see Figures 2B and S6A). This suggests that progressive memory impairments have distinct neural correlates from the onset and frequency of epileptic activity.

#### Early-onset desynchronization in the HPC of epileptic mice

To determine how synchronization of the hippocampal-entorhinal circuit is disrupted across the progression of memory deficits in epilepsy, we performed *in vivo* acute extracellular electrophysiological recordings using high-density silicon probes in awake, behaving, head-fixed mice. In a new cohort of animals, we recorded simultaneously from the HPC and MEC of control and epileptic male mice at 3 or 8 weeks after Pilo-SE as mice navigated a virtual linear track (Figure 2A). We also performed chronic wireless electroencephalogram (EEG) recordings for three weeks prior to silicon probe recordings to examine the onset of chronic seizures. All pilocarpine-treated mice showed spontaneous seizures throughout the EEG recording period, and we found no differences in the frequency of seizures recorded in the 3-week epileptic or 8-week epileptic mice (Fig-

ure 2B). No seizures were observed in control mice. To engage spatial processing during silicon probe recordings, mice were head-fixed atop a Styrofoam ball and trained to run through a virtual reality (VR) linear track for water rewards.<sup>35</sup> After animals were well-trained (8–12 total sessions), we performed dual-region acute electrophysiology recordings with two 256-channel silicon probes (4 shanks with 64 channels per shank) by lowering one probe into the dorsal HPC and the other into the superficial layers of MEC (Figure 2C). Example local field potential (LFP) traces for each subregion in the HPC and MEC are shown in Figure 2D, and probe tracts from each animal are shown in Figure S3. To isolate hippocampal processing, we limited our analysis to periods of locomotion. We found no differences in running speed between any of the groups (Figure S4A), consistent with our previous work.<sup>35</sup> In addition, control mice in the 3-week and 8-week groups had no differences in theta power (Figure S4B) or theta coherence (Figures S4C and S4D) and were therefore combined for all further analyses.

We first examined the time course of intra-HPC synchronization deficits, which have been previously found in multiple models of epilepsy.<sup>35,41</sup> We measured theta power and coherence along the CA1-DG axis, as well as theta phase locking (the propensity of a neuron to be active at a specific phase of theta oscillations<sup>35</sup>) of inhibitory neurons in the HPC. Together, these measures reflect the degree of coordination between long-range inputs and local neural activity in the HPC.<sup>77,78</sup> At

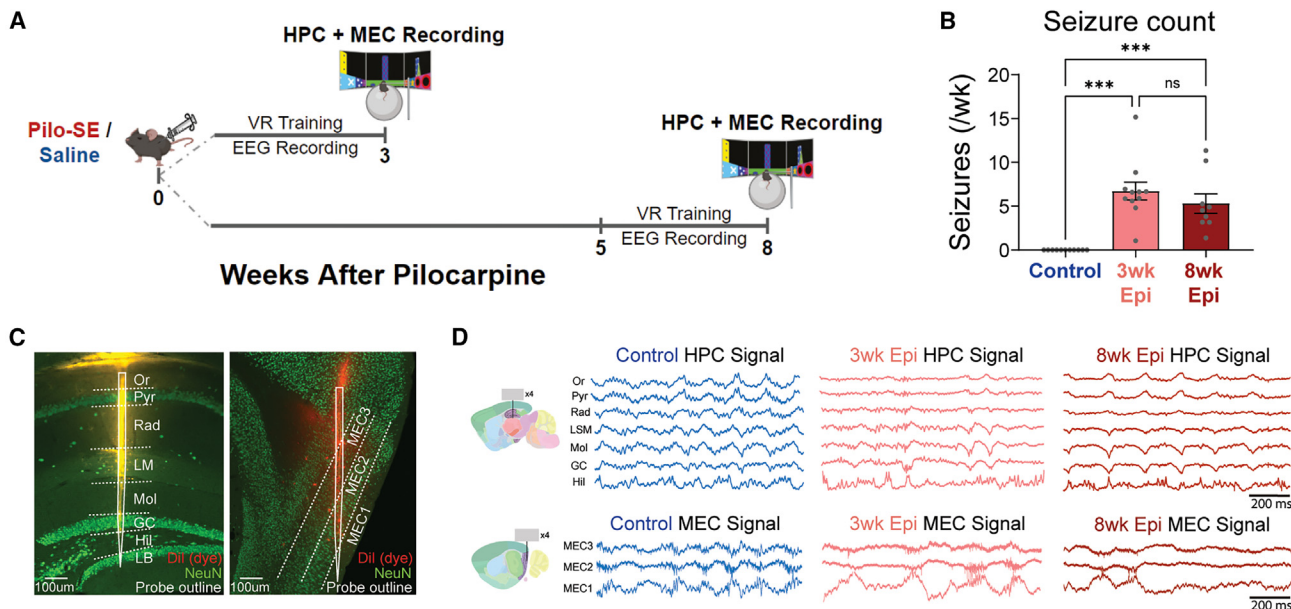


**Figure 2. Simultaneous *in vivo* electrophysiology of HPC and MEC in control and epileptic mice 3 or 8 weeks after Pilo-SE**

(A) Schematic of experimental timeline. Simultaneous hippocampus (HPC) and medial entorhinal cortex (MEC) recordings were performed in head-fixed mice 3 or 8 weeks after Pilo-SE or saline injection. During recordings, animals ran through a virtual linear track for water rewards.

(B) Chronic wireless EEG prior to silicon probe recordings showed that seizure frequency was not significantly different between 1–3 and 6–8 weeks after Pilo-SE. (C) Silicon probes were inserted into dorsal HPC (spanning CA1 and dentate gyrus) and MEC (spanning from MEC3 to MEC1). Probes were covered with Dil (DilC<sub>18</sub>(3)) prior to recordings to facilitate later visualization of the probe tracts. Scale bars, 100  $\mu$ m.

(D) Example signals from each layer of HPC and MEC during recording in control, 3-week epileptic, and 8-week epileptic groups. Scale bars, 200 ms. Or, stratum oriens; Pyr, stratum pyramidale; Rad, stratum radiatum; LM, stratum lacunosum moleculare; Mol, molecular layer; GC, granule cell layer; Hil, hilus; LB, lower blade.

Error bars represent SEM \*p < 0.05, \*\*\*p < 0.001. See also Figures S3 and S5.

both 3 weeks and 8 weeks after Pilo-SE, epileptic animals showed reduced theta power in the lacunosum moleculare (LM) layer of CA1 and the molecular layer (Mol) of the DG (Figure 3A). These sublayers correspond to the inputs from entorhinal cortex, and reduced power may reflect reduced input strength or coordination in epileptic mice. We next examined HPC theta coherence across each recorded channel pair. At 3 weeks after Pilo-SE, we found decreased theta coherence between CA1 and DG as well as within DG (Figure 3B), with the most prominent reductions occurring between DG Hil and CA1 stratum oriens (Or), CA1 LM, DG Mol, and DG granular cell layer (GC). By 8 weeks after Pilo-SE, we found additional deficits in coherence between DG Hil and CA1 stratum pyramidale (Pyr) (Figure 3B). These theta coherence deficits reflect reduced coordination of hippocampal processing across CA1 and DG in epileptic mice. Importantly, both deficits in hippocampal theta power and coherence primarily emerged early, within 3 weeks of Pilo-SE, which aligned with early-onset relatively minor memory impairment on the NOL task (Figure 1).

Reduced theta power and coherence in epileptic mice could be a result of recent seizures that disrupted neural activity. To address this possibility, we examined the correlation between theta power or coherence and seizure frequency or seizure recency (time between the last seizure and the recording). We found that decreased HPC theta power and coherence in epileptic mice were not significantly correlated with seizure frequency or

recency (Figures S5A–S5D), suggesting that hippocampal theta power and coherence deficits are unrelated to seizure susceptibility. Furthermore, to investigate whether the burden of IEDs correlates with theta changes in epileptic animals, we first looked into IED counts during running and non-running periods and found that the vast majority of interictal discharges occurred during non-running epochs (Figure S6B), suggesting they are highly unlikely to impact our electrophysiology results, which were restricted to periods of locomotion. In addition, IED frequency was not significantly correlated with decreased HPC theta power and coherence in epileptic mice (Figures S6C–S6F).

We previously found that interneurons in the DG have abnormal phase locking relative to theta oscillations in epileptic mice 17+ weeks after Pilo-SE.<sup>35</sup> This abnormal phase locking is independent of deficits in theta power<sup>35</sup> and may contribute to abnormal spatial processing in epileptic mice.<sup>79,80</sup> To examine the time course of these phase locking deficits, we first isolated single units from our recordings and identified putative interneurons based on firing properties<sup>33,35,81</sup> (Figure S7, see STAR Methods). We then calculated the mean phase of firing ( $\mu$ ) and phase locking strength ( $r$ ) for each interneuron.<sup>35</sup> In control mice, DG interneurons were reliably phase locked near the trough of CA1 theta. However, in epileptic mice at both 3 and 8 weeks after Pilo-SE, we found an altered distribution of preferred firing phases ( $\mu$  values), with individual DG interneurons preferentially active across the theta cycle (Figure 3C). The

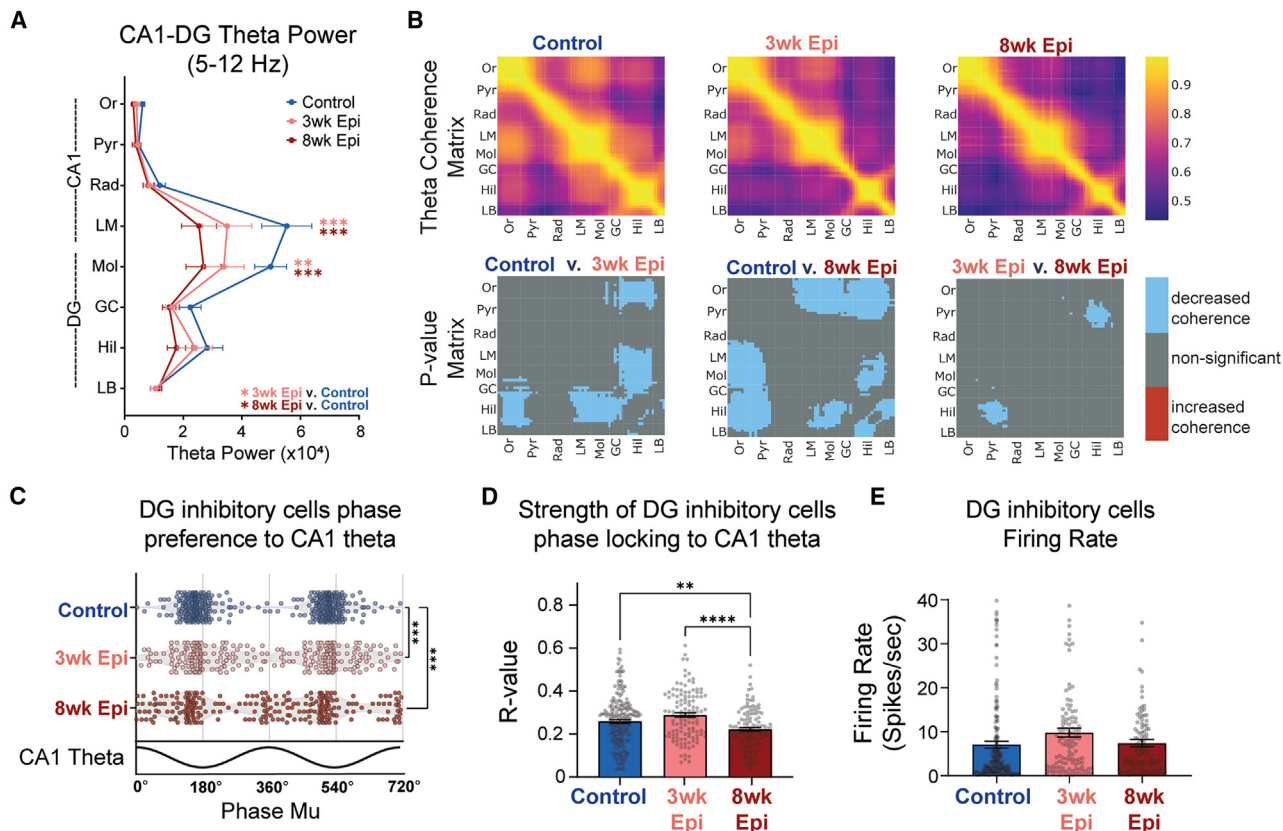


**Figure 3. Deficits in HPC synchronization primarily emerge by 3 weeks after Pilo-SE**

(A) Theta power recorded from each hippocampus layer. Epileptic animals had reduced power in LM and Mol layers in both 3-week and 8-week epileptic groups. (B) Theta coherence between each channel pair along the probe in HPC in control (top left), 3-week epileptic (top middle), and 8-week epileptic (top right) mice. *p* value matrix (bottom row) of significant changes in coherence at each location between experimental groups (blue: decreased coherence; red: increased coherence). Both 3-week and 8-week epileptic groups showed reduced theta coherence between CA1 and DG, with progressively decreased theta coherence between Pyr and Hil from 3 weeks to 8 weeks after Pilo-SE.

(C) Phase preference to CA1 theta for DG interneurons in control and epileptic animals. Each dot represents one interneuron, and data are double plotted for visualization purposes. Both 3-week epileptic and 8-week epileptic groups showed disrupted phase preferences compared to control.

(D) Phase locking strength (*R* value) of DG interneurons to CA1 theta. 8-week epileptic group showed reduced phase locking strength compared to both control and 3-week epileptic group.

(E) No differences in firing rate of DG inhibitory cells.

Or, stratum oriens; Pyr, stratum pyramidale; Rad, stratum radiatum; LM, stratum lacunosum moleculare; Mol, molecular layer; GC, granule cell layer; Hil, hilus; LB, lower blade.

Error bars represent SEM \**p* < 0.05, \*\**p* < 0.01, \*\*\**p* < 0.001, \*\*\*\**p* < 0.0001 for (A), (D), and (E); \**p* < 0.017, \*\**p* < 0.003, \*\*\**p* < 0.0003 for (C). See also Figures S4 and S7.

strength of phase locking (*r*) was also slightly reduced in the epileptic mice, but only at 8 weeks after Pilo-SE (Figure 3D). Notably, the firing rates of DG inhibitory neurons were unaltered either 3 or 8 weeks after Pilo-SE (Figure 3E), suggesting that the frequency of inhibitory firing was unchanged, but the timing relative to theta was disrupted. Overall, DG interneurons had disrupted theta phase locking early after epileptogenesis, primarily occurring within the first 3 weeks after Pilo-SE, similar to what we observed with HPC theta power and coherence (Figures 3A and 3B). Together, these data demonstrate that HPC theta synchronization and spike timing are largely disrupted within the first 3 weeks of epileptogenesis, matching the timeline of early minor memory deficits (Figures 1C and 1E) and the onset of seizures (Figure 2B).

#### Late-onset deficits in the timing of MEC excitatory inputs to HPC in epileptic mice

Given the substantial theta synchronization deficits we observed in HPC of epileptic mice, we next examined the timing of upstream inputs from MEC. Excitatory neurons in MEC2 and MEC3 project into the HPC<sup>54</sup> and strongly drive HPC theta.<sup>81</sup> Therefore, it is possible that abnormal spike timing or reduced activity in these populations could underlie the HPC theta desynchronization we found at 3 and 8 weeks after Pilo-SE. To test this hypothesis, we isolated excitatory neurons in MEC2 and MEC3 (Figure S7) and examined their theta phase locking. Since MEC2 neurons project directly to the DG, we examined the phase locking of these neurons to DG theta oscillations. By referencing to theta oscillations in the downstream HPC target

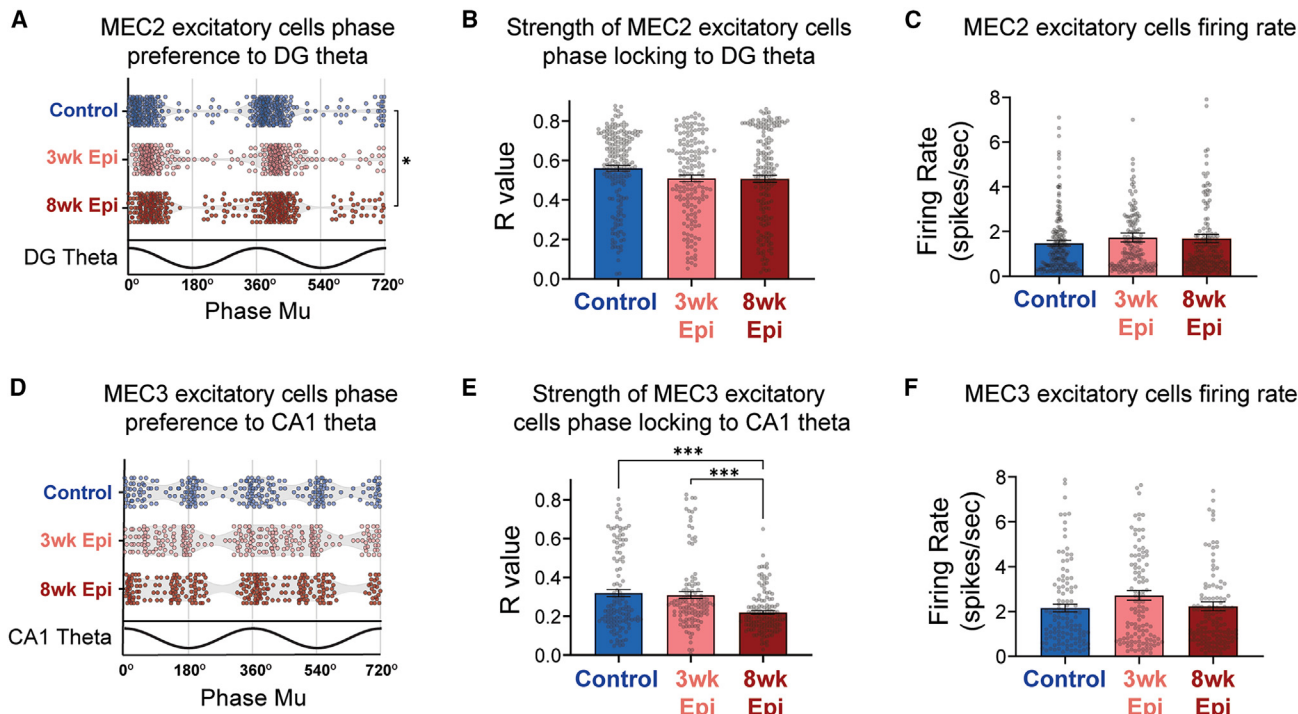


**Figure 4. MEC3 single units show late-onset reduction in theta phase locking strength**

- (A) Phase preference to DG theta for MEC2 excitatory cells in control and epileptic animals.
- (B) No changes in phase locking strength of MEC2 excitatory cells to DG theta in epileptic mice.
- (C) No changes in firing rate of MEC2 excitatory cells in epileptic mice.
- (D) No changes in phase preference to CA1 theta for MEC3 excitatory cells in control and epileptic animals.
- (E) Reduced phase locking strength of MEC3 excitatory cells to CA1 theta in epileptic mice 8 weeks after Pilo-SE.
- (F) No changes in firing rate of MEC3 excitatory cells in epileptic mice.

Error bars represent SEM \* $p < 0.05$ , \*\* $p < 0.01$ , \*\*\* $p < 0.001$  for (B), (C), (E), and (F); \* $p < 0.017$  for (A) and (D). See also Figures S7 and S8.

region, we can assess how MEC spikes are coordinated with HPC processing. At 3 weeks after Pilo-SE, we found that theta phase locking of MEC2 excitatory cells was intact in epileptic animals, with no changes in the distribution of theta phase preference (Figure 4A), phase locking strength (Figure 4B), or firing rate (Figure 4C). At 8 weeks after Pilo-SE, we saw similar results, with the exception of a relatively small change in the concentration of theta phase preferences (Figure 4A). Together, these results suggest that changes in MEC2 theta phase locking are unlikely to contribute to the early theta desynchronization observed in HPC at 3 weeks after Pilo-SE.

We next examined the phase locking of MEC3 excitatory neurons to CA1 theta, as these neurons project directly to CA1. We found no significant changes in the distribution of phase preferences at either 3 or 8 weeks after Pilo-SE (Figure 4D). However, we did find a late-onset reduction in phase locking strength in epileptic mice at 8 weeks after Pilo-SE (Figure 4E), suggesting a breakdown in the precise timing of MEC3 excitatory neuron spiking during the progression of epileptogenesis. No firing rate changes were detected in this population at either time point (Figure 4F), again suggesting that overall activity levels were maintained but that changes were occurring primarily in the timing of this neural activity. Together, these results indicate that MEC excitatory activity in both layers 2 and 3 was intact at

the early time point (3 weeks after Pilo-SE) when HPC deficits and minor memory impairment were already observed. Therefore, changes in MEC unit activities are unlikely to drive HPC deficits. However, we did observe late-onset MEC phase-locking deficits, primarily in the strength of phase locking in MEC3 excitatory neurons to downstream CA1 theta, which match the time course of progressive memory deficits.

To further explore the activity of individual neurons in MEC, we examined the firing properties of MEC inhibitory cells relative to local MEC theta. We found minimal changes in theta phase locking of MEC2 and MEC3 inhibitory neurons in epileptic mice (Figure S8). We did, however, find an increase in firing rate of MEC2 inhibitory cells in 8-week epileptic mice (Figure S8C), suggesting that inhibitory function is also altered in the MEC of epileptic mice 8 weeks after Pilo-SE.

#### Deficits in MEC3 spike timing are driven by a distinct subpopulation that is preferentially active at the trough of MEC theta

While MEC3 excitatory neurons are often thought to be a homogenous population, there is some evidence of distinct subpopulations that are active at different phases of theta oscillations.<sup>32,82</sup> Indeed, we observed two clusters of phase preferences in MEC3 excitatory neurons in all groups of animals (Figure 4D). To gain

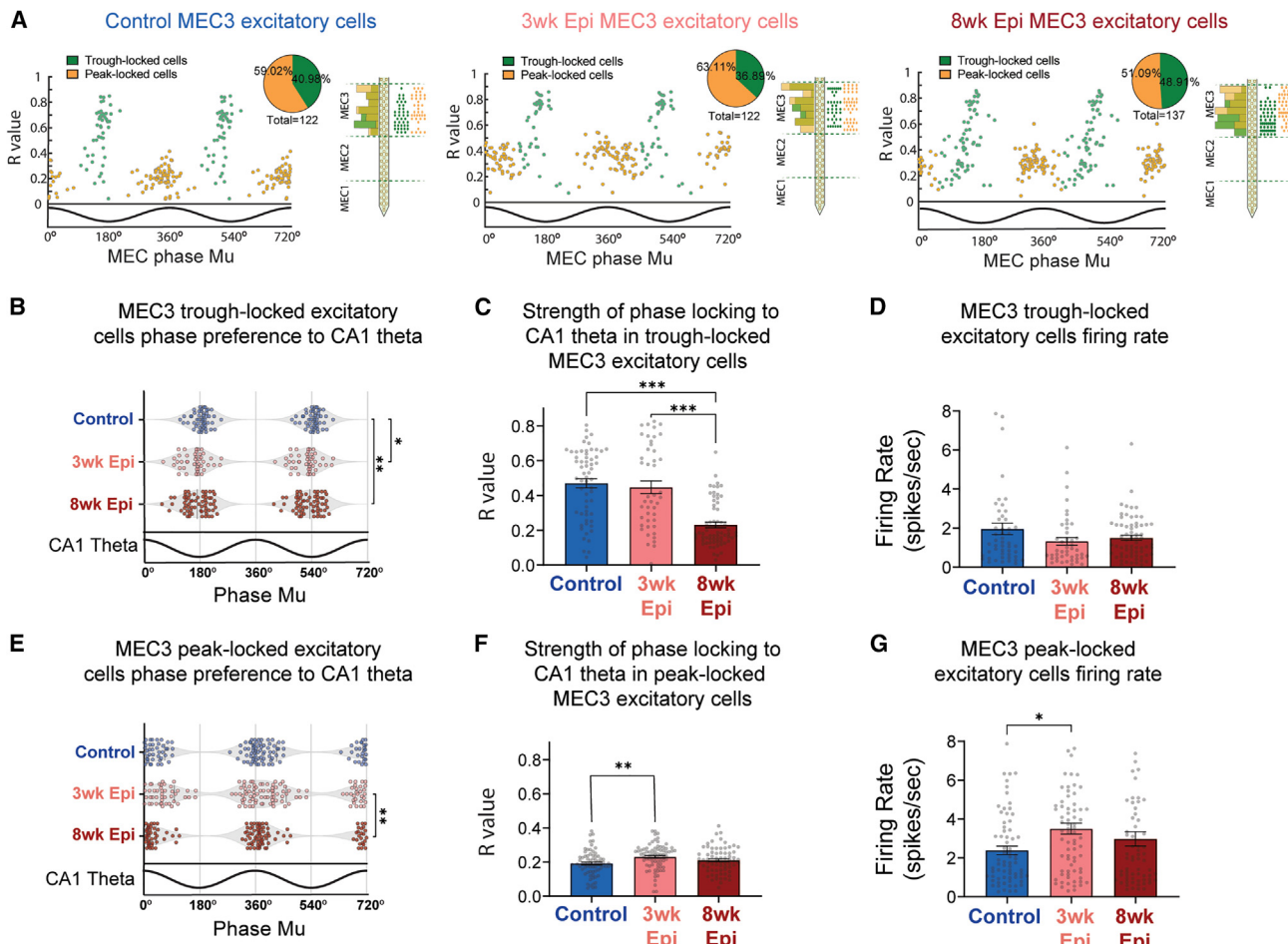


**Figure 5. Reduced theta phase locking is specific to a subpopulation of trough-locked MEC3 excitatory units**

(A) MEC3 excitatory cells show two distinct clusters based on their theta phase preference to local theta (x axis) and phase locking strength (y axis). K-means clustering was used to separate the two populations into trough-locked units (green) and peak-locked units (orange). Right side plots show the distribution of the 2 clusters along the probe in each group.

(B) Altered distribution of phase preferences to CA1 theta for MEC3 trough-locked excitatory units in epileptic mice. Each data point represents one single-unit, and data are double plotted for visualization.

(C) Reduced phase locking strength of MEC3 trough-locked excitatory units to CA1 theta in 8-week epileptic mice.

(D) No changes in firing rate of MEC3 trough-locked excitatory units in epileptic mice.

(E) Phase preference to CA1 theta for MEC3 peak-locked excitatory units in control and epileptic animals.

(F) Increased phase locking strength of MEC3 peak-locked excitatory cells to CA1 theta in epileptic mice 3 weeks after Pilo-SE.

(G) Increased firing rate of MEC3 peak-locked excitatory cells in epileptic mice 3 weeks after Pilo-SE.

Error bars represent SEM \* $p < 0.05$ , \*\* $p < 0.01$ , \*\*\* $p < 0.001$  for (C), (D), (F), and (G); \* $p < 0.017$ , \*\* $p < 0.003$  for (B) and (E). See also Figure S9.

more insights into these subpopulations of MEC3 excitatory cells, we performed k-means clustering on their preferred phase (mu) and phase locking strength ( $r$ ) to the local MEC theta, and these cells fell into two distinct clusters (Figures 5A and S9G). Within each experimental group, the clusters reliably formed two populations, with one active primarily at the theta trough (trough-locked) and one primarily active at the theta peak (peak-locked). We found no difference in the spatial distribution of these clusters along the silicon probe (Figure 5A), indicating that these two cell populations are evenly dispersed throughout MEC3 and that this effect is not due to cells being picked up from neighboring regions above or below MEC3. We also further char-

acterized the firing properties of the MEC3 trough-locked and peak-locked cells and found that they differ in waveform shape and burst index (Figures S9A–S9F), reinforcing that they are indeed distinct subpopulations of MEC3 neurons.

We then investigated how each subpopulation of MEC3 excitatory neurons was phase locked to downstream CA1 theta. While initial clustering was performed using local MEC theta as a reference (Figure 5A), we examined the synchronization of these neurons to downstream CA1 theta because this is their primary output region. We found that the trough-locked MEC3 neurons were specifically altered in epileptic mice (Figure 5) and fully accounted for the reduced phase locking strength observed in the full population

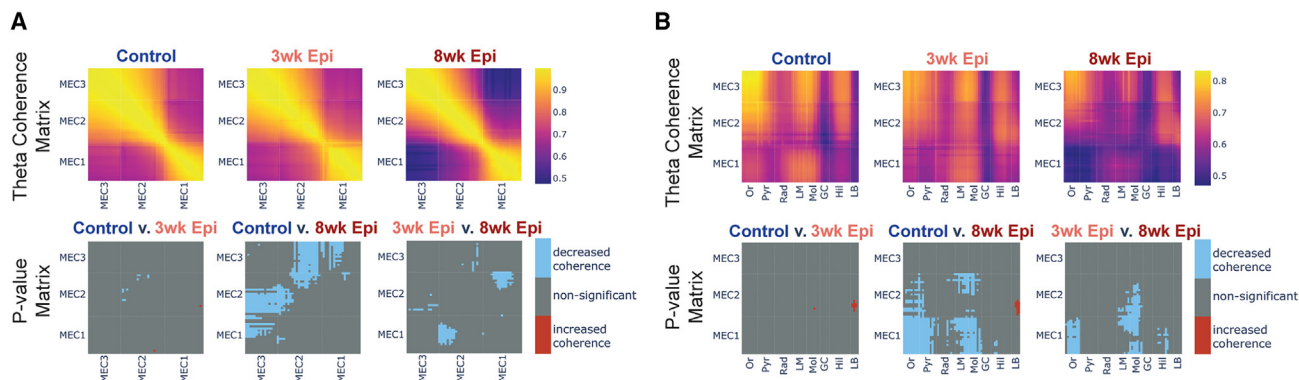


**Figure 6. Decreased theta coherence within the MEC and between MEC and HPC emerges between 3 and 8 weeks after Pilo-SE**

(A) Theta coherence between each channel pair along the probe in MEC in control (top left), 3-week epileptic (top middle), and 8-week epileptic (top right) mice.  $p$  value matrix (bottom row) shows significant changes in coherence at each location between experimental groups, with reduced coherence emerging by 8 weeks after Pilo-SE.

(B) Theta coherence between each channel pair along the probe in MEC and HPC in control (top left), 3-week epileptic (top middle), and 8-week epileptic (top right) mice.  $p$  value matrix (bottom row) shows significant changes in coherence at each location between experimental groups, with reduced coherence emerging by 8 weeks after Pilo-SE.

Or, stratum oriens; Pyr, stratum pyramidale; Rad, stratum radiatum; LM, stratum lacunosum moleculare; Mol, molecular layer; GC, granule cell layer; Hil, hilus; LB, lower blade.

(Figure 4E). In epileptic mice, trough-locked cells showed more dispersed phase preferences to CA1 theta in both 3-week and 8-week epileptic groups (Figure 5B). However, the strength of theta phase locking ( $r$ ) was substantially reduced only in the 8-week epileptic group (Figure 5C). These changes were not driven by changes in overall activity as we found no differences in the firing rate of trough-locked neurons (Figure 5D). In the peak-locked cluster, the distribution of preferred phases was similar between the control group and both epileptic groups (Figure 5E). In addition, there was a small, but statistically significant, increase in phase locking strength to CA1 theta (Figure 5F) as well as in the firing rate (Figure 5G) of MEC3 peak-locked excitatory cells in 3-week epileptic animals. Notably, these opposing results in MEC3 peak-locked and trough-locked excitatory cells suggest that the observed effects are not due to changes in the downstream CA1 theta oscillation but rather reflected specific changes to the timing of these distinct MEC3 cell types. To rule out potential bias in the k-means clustering method used on MEC3 excitatory cells across different groups (Figure 5A), we also separated MEC3 excitatory units into trough-locked and peak-locked neurons based entirely on whether their preferred firing phase was closer to the peak or trough of MEC theta (Figure S9G). Using this approach, we again found reduced phase locking strength of trough-locked MEC3 excitatory cells to CA1 theta in 8-week epileptic mice (Figures S9H–S9K). Together, these results indicate that the late-onset deficits in the strength of MEC3 excitatory cell phase locking in epileptic mice (Figure 4E) are driven entirely by the trough-locked subcluster. These results suggest that this unique subpopulation may be specifically vulnerable during the progression of epilepsy and highlight the need for further investigation into these cell types.

Notably, data examining single-unit phase locking strength (Figures 3D, 4B, 4E, 5C, and 5F) were collapsed across animals due to variability in the number of cells recorded per animal, which prevented a reliable estimate of the distribution of values

for each subject. However, to increase the robustness of our analysis, we also performed a more conservative nested analysis that includes subject as a factor. Critically, the primary finding that MEC3 trough-locked excitatory neurons have a progressive deficit in phase locking strength in 8-week epileptic mice (Figure 5C) survives this more conservative approach (see statistical results in Table S1). For all other comparisons of phase locking strength (Figures 3D, 4B, 4E, and 5F) this conservative approach did not reach significance.

#### Progressive deficits in theta coherence within the MEC and between MEC-HPC emerge between 3 and 8 weeks after Pilo-SE

Both HPC and MEC are required for successful spatial memory performance, and theta synchrony within and between these regions is key to proper spatial processing.<sup>27–29,83,84</sup> Therefore, we examined theta coherence within the MEC and between MEC and HPC across the progression of memory deficits from 3 to 8 weeks after Pilo-SE. We found that theta coherence between MEC2 and MEC3 was fully intact at 3 weeks after Pilo-SE but was reduced by 8 weeks after Pilo-SE (Figure 6A). Similarly, we also found reduced theta coherence between MEC and HPC at 8 weeks after Pilo-SE that was not present at the 3-week time point (Figure 6B). Specifically, by 8 weeks after Pilo-SE, we found reduced theta coherence between MEC1/MEC2 and Or, Pyr, LM, and Mol of HPC (Figure 6B). Notably, these deficits in long-range coherence were restricted to MEC1 and MEC2, with no significant changes in MEC3 coherence with the HPC. Together, these data suggest that deficits in theta synchrony within the MEC and between the MEC and HPC emerge between 3 and 8 weeks after Pilo-SE, during the period when spatial memory impairments are becoming more severe (Figures 1C and 1D).

To test whether these theta coherence deficits in the MEC and between the MEC and HPC were related to seizure

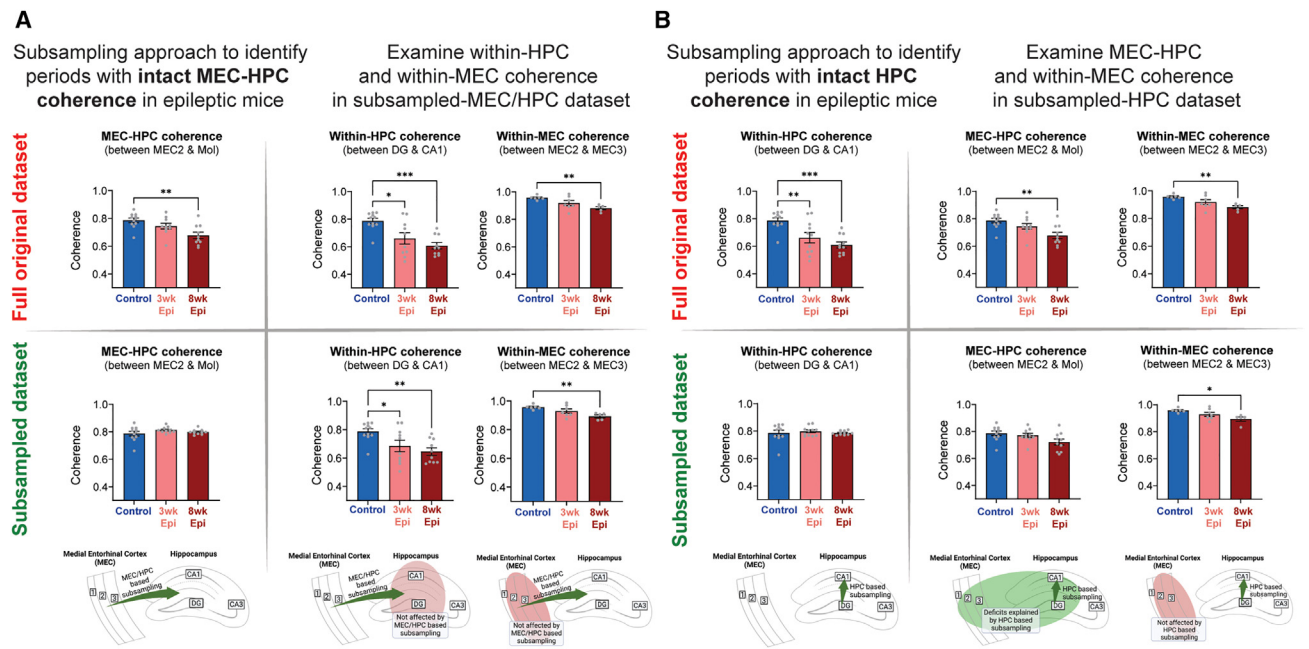


**Figure 7. Subsampling approach reveals dissociation between local and long-range theta coherence deficits in epileptic mice**

(A) Using a subsampling approach, we identified a set of time bins with equivalent theta coherence between MEC-HPC in all groups (left column). Using the full original dataset, theta coherence was reduced within-HPC and within-MEC in epileptic mice (top right). In the subsampled-MEC/HPC dataset (bottom row) with no deficits in MEC-HPC coherence, within-HPC and within-MEC theta coherence deficits were still present in epileptic mice.

(B) Using a similar subsampling approach, we identified a new set of time bins with equivalent theta coherence within-HPC in all groups (left column). In the full original dataset, theta coherence was reduced between MEC-HPC (top middle) and within-MEC (top right). In the subsampled-HPC dataset (bottom row) with no deficits in within-HPC theta coherence across groups, there were no deficits in long-range MEC-HPC coherence in epileptic mice, but within-MEC theta coherence deficits were still present in epileptic mice.

Error bars represent SEM \* $p < 0.05$ , \*\* $p < 0.01$ , \*\*\* $p < 0.001$ . See also Figure S10.

susceptibility, we examined the correlation between theta coherence and seizure frequency and seizure recency. We found that the coherence within the MEC or between MEC-HPC was uncorrelated with both seizure frequency and seizure recency (Figures S5E–S5H), suggesting that these theta coherence deficits are not directly associated with seizure susceptibility.

#### Dissociation of long-range MEC-HPC theta coherence from local HPC or MEC coherence deficits

In our recordings, we found several synchronization deficits in epileptic mice, but little is known about how these deficits may impact each other. To investigate the relationship between local theta coherence deficits within the HPC or MEC and long-range deficits between the two regions, we used a subsampling approach to determine whether these effects could be dissociated. In the 3-week and 8-week epileptic animals, we selected a subset of time bins that had MEC-HPC theta coherence levels equivalent to controls. This led to a new “subsampled-MEC/HPC” dataset with similar MEC-HPC coherence across all groups (Figures 7A and S10, see STAR Methods). We then tested whether theta coherence within the MEC or within the HPC was still reduced in the epileptic animals compared to controls in this subsampled dataset. We found that theta coherence deficits within the HPC

and within the MEC persisted in epileptic animals in the subsampled-MEC/HPC dataset (Figure 7A), despite similar cross-region coherence to controls during the subsampled periods. This indicates that long-range theta synchrony between MEC-HPC can be dissociated from within-region coherence.

Similarly, we next created a second subset of time bins in the epileptic animals that had levels of theta coherence within the HPC (between DG and CA1) equivalent to controls. This led to a “subsampled-HPC” dataset that had similar within-HPC coherence across all groups (Figure 7B). We then tested whether epileptic mice continued to have reduced coherence between MEC-HPC or within the MEC in this dataset. Surprisingly, we found that epileptic mice did not have a deficit in MEC-HPC theta coherence within this subsample (Figure 7B, middle panel). That is, in epileptic mice, periods of normal theta coherence within the HPC were associated with normal levels of MEC-HPC theta coherence. This suggests that there is an intact theta generator in epileptic mice, even at 8 weeks after Pilo-SE, which can drive coherent theta within the HPC and between the HPC and MEC but does so only in a subset of time bins. However, during this subsampled-HPC dataset, we also found that theta coherence deficits within the MEC persisted in epileptic animals (Figure 7B, right panel), suggesting that theta coherence within the MEC can be further dissociated from theta coherence in the HPC and between the HPC and MEC.

To further investigate the brain states that produced intact levels of theta coherence, we performed a detailed characterization of within-HPC, within-MEC, and MEC-HPC coherence-based subsampling ([Figure S10](#)). Overall, we found that all three subsamples were associated with high levels of running speed, were less likely to occur during run initiation, and were evenly distributed across the virtual track, except for the first spatial bins that are associated with run initiation ([Figure S10](#)).

## DISCUSSION

Together, our work demonstrates that there is a progression of HPC and MEC circuit deficits that arise following epileptogenesis and accumulate as spatial memory impairment worsens. We found that deficits in hippocampal theta and interneuron spike timing emerged early, within 3 weeks after Pilo-SE ([Figure 3](#)), while deficits in MEC spike timing, within-MEC theta coherence, and coherence between MEC and HPC emerged later, by 8 weeks after Pilo-SE ([Figures 4, 5, and 6](#)). In particular, a distinct subpopulation of trough-locked MEC layer 3 excitatory neurons was specifically impaired in epileptic mice. This progression of theta synchronization and spike timing deficits occurred at the same time point as progressive deficits in spatial memory ([Figures 1C and 1D](#)). Notably, seizures, IEDs, and cell death occurred early after Pilo-SE and did not increase across the same time course as progressive memory deficits ([Figures 2B, S2, and S6A](#)). Finally, we found that changes in long-range MEC-HPC theta coherence are dissociable from within-region theta coherence deficits in epileptic mice ([Figure 7A](#)) and that there were periods of time when theta coherence within the HPC and between MEC-HPC were both intact in epileptic mice ([Figure 7B](#)).

### Progressive memory deficits in epileptic mice are dissociable from seizures and cell death

Memory deficits are well established in epilepsy, but little is known about how they progress and which specific circuits are involved in producing these memory impairment. We found that epileptic mice had mild, early-onset memory deficits that progressively worsened after Pilo-SE ([Figure 1](#)). These results reinforce the notion that there is an accumulated breakdown of spatial memory circuits in epileptic mice that contribute to altered memory performance. Meanwhile, seizure frequency, IED frequency, and cell death did not progress from 3 to 8 weeks after Pilo-SE ([Figures 2B, S2, and S6A](#)), suggesting that they are unlikely to drive the progression or worsening of these memory deficits at the later time point. However, it remains possible that the cumulative number of seizures, rather than the onset or frequency, could impact memory performance. Future work using novel approaches to inhibit seizures in this model could examine whether cumulative seizure activity directly contributes to the progression of memory impairment after Pilo-SE. Similarly, it remains possible that the indirect effects of cell death (e.g., compensatory excitability changes, axonal sprouting, and altered connectivity) may emerge over time and still contribute to progressive memory impairment. Importantly, epileptic mice often have substantial variability in the symptoms induced by Pilo-SE, and we did observe substantial variability in behavior in our epileptic mice (e.g., [Figure 1E](#)). While there was substantial

variability in the distribution of test scores, our results clearly indicate a severe memory deficit in the epileptic mice. It is possible that the high levels of variability observed in epileptic animals may be due to these animals having an increased propensity to be biased toward one object or the other during testing, possibly due to increased anxiety.<sup>62,85</sup> However, any subject that was heavily biased during training was removed from the dataset and thus this could not be a primary driver of the behavioral deficit we observed.

### The HPC is an early site of abnormal synchronization in epileptic mice

Three weeks after Pilo-SE, we found theta power, coherence, and phase-locking deficits in epileptic mice that were predominantly restricted to the HPC ([Figure 3](#)). These changes were independent of upstream changes in the MEC, as MEC theta oscillations and spike timing were mostly intact at this time point ([Figures 4, 5, and 6](#)). This suggests that early deficits may be driven by HPC-specific changes such as rewiring of HPC connections or altered long-range inputs to HPC. However, it also remains possible that other properties of MEC neurons besides spike timing could be disrupted including reduced MEC axon targeting of HPC, altered spike fidelity, or disrupted neurotransmitter release. Notably, our silicon probes were not able to reliably record from dentate granule cells to determine their firing activity, but future experiments could provide additional insight into how this critical population is altered in epileptic mice.

The time course of early HPC desynchronization aligns with poor spatial memory on the “hard” NOL task ([Figure 1](#)) and reduced precision of spatial coding in CA1.<sup>35</sup> Interestingly, even after the onset of major synchronization deficits, we found that, during periods with high within-HPC theta coherence, there were also high levels of synchronization between MEC-HPC ([Figure 7B](#)). Therefore, HPC coherence may be a reliable biomarker for periods of relatively “normal” cognitive function and could be used to inform neurofeedback interventions or even be targeted to restore theta across the HPC and MEC after epileptogenesis.

### Synchronization deficits in the MEC emerge as memory impairment progresses in epileptic mice

Deficits in neural synchrony within the MEC and between MEC-HPC predominantly emerged between 3 and 8 weeks after Pilo-SE ([Figures 4, 5, and 6](#)). This late-onset dysfunction of MEC circuits had a similar time course to the progression of memory deficits on the NOL task and the onset of impaired CA1 spatial stability.<sup>35</sup> Given the extensive evidence that the timing of direct entorhinal inputs to CA1 can mediate plasticity of CA1 neurons,<sup>86–89</sup> this suggests that disrupted timing of MEC3 excitatory neurons may be an important mediator of CA1 instability and memory deficits in epilepsy. For instance, behavioral timescale synaptic plasticity is sufficient to form spatial maps and relies on temporally precise convergent inputs from MEC3 and CA3 to induce new stable place fields in CA1.<sup>86–89</sup> Therefore, in epileptic mice, the disrupted MEC-HPC theta synchrony may directly impair the development of stable place fields. Given that theta oscillations primarily reflect synchronized excitatory inputs, the altered theta coherence between

the HPC and MEC may reflect broader brain-wide desynchronization, perhaps driven by disrupted long-range synchronization mechanisms.

### A theta trough-locked excitatory population in MEC3 may be selectively vulnerable in epilepsy

We found clear evidence of distinct subpopulations of trough-locked and peak-locked MEC3 excitatory neurons<sup>32</sup> in both control and epileptic mice (Figure 5A). Furthermore, we found a subtype-specific deficit in theta phase locking in the trough-locked MEC3 neurons of epileptic mice 8 weeks after Pilo-SE (Figure 5C). This deficit emerged between 3 and 8 weeks after Pilo-SE, suggesting it may be linked to the progressive memory deficits observed at this later time point. Deficits in trough-locked MEC3 excitatory neurons may contribute to memory impairment by disrupting predictive coding in CA1 of epileptic mice. MEC3 neurons input directly into CA1, and recent evidence suggests that they are necessary for temporal coding, such as phase precession of CA1 neurons,<sup>85,90</sup> which is disrupted in chronically epileptic mice.<sup>36</sup> Furthermore, trough-locked MEC3 excitatory neurons appear to provide key predictive information about spatial location that is critical for the predictive coding of position during navigation.<sup>82</sup> Thus, the deficits we observed in MEC3 trough-locked neurons are likely to disrupt predictive codes in CA1, and this may directly impair cognitive performance.

Notably, previous studies have found hyperexcitability in MEC2 circuits in epileptic rats using *ex vivo* brain slices,<sup>91–93</sup> as well as increased excitatory inputs from the MEC to the DG that may drive chronic seizures in a Dravet Syndrome mouse model.<sup>94,95</sup> However, in the present study, we did not observe increased firing rates in MEC2 or MEC3 excitatory neurons *in vivo*, suggesting that compensatory mechanisms, such as increased local MEC inhibitory inputs, may normalize firing patterns in the MEC in the Pilo-SE model. In line with this, we did observe increased firing rates of inhibitory neurons in MEC2 of 8-week epileptic mice (Figure S8C). Furthermore, since there are multiple excitatory cell types in MEC2 and we did not have cell-type specificity in our recordings, it remains possible that specific changes to the HPC-projecting stellate cells could be occluded by changes in other cell types (i.e., MEC2 pyramidal cells).

### Dissociable circuit mechanisms drive within- and cross-region theta coherence deficits

To examine how deficits within and between the HPC and MEC might be related, we performed a subsampling analysis to determine if periods of intact cross-region theta coherence (MEC-HPC) were associated with normal within-region coherence (Figures 7A and S10). If within- and cross-region coherence deficits were controlled by a single network mechanism (e.g., collateral long-range inputs), then they should be correlated in time throughout the recording. However, we found a clear dissociation between these deficits in epileptic mice, suggesting that distinct networks were contributing to local and long-range desynchrony. This suggests that MEC-HPC coherence is not sufficient for downstream HPC coherence and that these within- and across-regions deficits can be dissociated. On the other hand, when we subsampled periods of normal within-HPC theta coher-

ence, we found that these periods were associated with normal levels of MEC-HPC coherence (Figure 7B). This suggests that there is a theta generation mechanism that can influence both the HPC and MEC that is relatively intact in epileptic mice but only drives intact entorhinal-hippocampal synchronization in a subset of time periods. There are several possible candidate mechanisms that could drive this intact theta in epileptic mice, including long-range projections from the medial septum or supramammillary nucleus, or feedback projections from CA1 to MEC. Notably, while we were able to identify periods of intact within-MEC coherence in epileptic mice (Figure S10B), the subsampling approach limited the number of subjects that could be used to examine other metrics in this subsample. Thus, due to limited sample size, we were unable to examine how within-HPC and MEC-HPC coherence were affected during the within-MEC subsampling periods.

### Limitations of the study

Our work is inherently limited by the correlational nature of neural recordings. However, by recording from multiple time points across the progression of memory impairment, we can draw important inferences about the relationship between circuit and behavioral deficits at each time point. To directly test the causal role of altered HPC-MEC synchronization in epilepsy, new experimental techniques that can manipulate network synchrony are needed. Emerging tools are now being developed to deliver electrical or optogenetic stimulation in phase with endogenous rhythms<sup>96,97</sup> and directly manipulate theta coherence<sup>97</sup> or phase locking.<sup>96</sup> Our work suggests that resynchronizing the timing of DG inhibitory neurons and trough-locked MEC3 neurons, or increasing theta coherence between MEC and HPC, may lead to improved memory in epileptic mice. Another important limitation is that we did not record neural activity during a memory task, but rather during head-fixed locomotion on a virtual linear track. This approach allowed us to record high-quality single units and LFPs from the HPC and MEC simultaneously in a large number of animals. While the NOL task may have distinct behavioral demands from spatial navigation, there is an increase in theta power specifically during periods of object interaction.<sup>98</sup> Thus, these tasks both engage theta processes and offer valuable insights into how MEC-HPC disruption may contribute to memory deficits in chronically epileptic mice.

### RESOURCE AVAILABILITY

#### Lead contact

Further information and requests for resources or raw data should be directed to the lead contact, Tristan Shuman ([tristan.shuman@mssm.edu](mailto:tristan.shuman@mssm.edu)).

#### Materials availability

This study did not generate new unique materials.

#### Data and code availability

- Data, including all LFP and spike data, are available online on the DANDI Archive (<https://dandiarchive.org>; dataset number 000638).
- All original code developed for analysis of these data is available at: <https://doi.org/10.5281/zenodo.14341007>.
- Any additional information required to re-analyze the data reported in this paper is available from the **lead contact** upon request.

## ACKNOWLEDGMENTS

We thank the Cai and Shuman labs for feedback and support throughout this project. This work was supported by the CURE Taking Flight Award, American Epilepsy Society (AES) Junior Investigator Award, R01NS116357, R01NS136590, and RF1AG072497 to T.S.; R01MH120162, DP2MH122399, and R56MH132959 to D.J.C.; AES Predoctoral Fellowship to Y.F.; F31AG069496 to L.M.V.; F99NS135813 to I.S.; F31NS134301 to P.A.P.; and F32NS116416, AES Postdoctoral Fellowship, and Simons Collaboration on Plasticity and the Aging Brain Transition to Independence Award to Z.C.W. Silicon probes were graciously provided by Dr. Sotiris Masmanidis, funded by NeuroNex Technology Hub, award number 1707408. We also thank BioRender for figure creation (Figures 2, 5, 7, and S10).

## AUTHOR CONTRIBUTIONS

Conceptualization, Y.F., Z.C.W., and T.S.; methodology, Y.F., L.P.-H., L.M.V., and T.S.; formal analysis, Y.F., Z.D., and T.S.; investigation, Y.F., K.S.D., Z.D., L.P.-H., V.P.-H., J.S., S.I.L., P.A.P., A.J., C.J.R., and N.N.K.; writing—original draft, Y.F. and T.S.; writing—review and editing, Y.F., Z.C.W., Z.T.P., L.M.V., D.J.C., and T.S.; funding acquisition, D.J.C. and T.S.; supervision, Y.F., Z.C.W., I.S., D.J.C., and T.S.

## DECLARATION OF INTERESTS

The authors declare no competing interests.

## STAR★METHODS

Detailed methods are provided in the online version of this paper and include the following:

- KEY RESOURCES TABLE
- EXPERIMENTAL MODEL AND STUDY PARTICIPANT DETAILS
  - Study design
  - Animals
- METHOD DETAILS
  - Wireless EEG and headbar implant surgical procedures
  - Pilocarpine-induced status epilepticus
  - Novel object location task
  - Virtual reality (VR) training
  - Craniotomy and ground implantation surgery
  - Acute silicon probe recordings
  - Histology confirmation of probe track
  - Post-processing and analysis of local field potential data
  - Single unit spike sorting and phase preference analysis
  - EEG seizure quantification
  - Interictal epileptic discharge (IED) quantification
  - Immunohistochemistry at different timepoints
- QUANTIFICATION AND STATISTICAL ANALYSIS

## SUPPLEMENTAL INFORMATION

Supplemental information can be found online at <https://doi.org/10.1016/j.celrep.2024.115131>.

Received: February 27, 2024

Revised: August 15, 2024

Accepted: December 11, 2024

Published: January 22, 2025

## REFERENCES

1. Lee, Y.-J., and Lee, J.S. (2013). Temporal lobe epilepsy surgery in children versus adults: from etiologies to outcomes. *Korean J. Pediatr.* 56, 275–281. <https://doi.org/10.3345/kjp.2013.56.7.275>
2. Bell, B., Lin, J.J., Seidenberg, M., and Hermann, B. (2011). The neurobiology of cognitive disorders in temporal lobe epilepsy. *Nat. Rev. Neurol.* 7, 154–164. <https://doi.org/10.1038/nrneurol.2011.3>
3. Lin, H., Holmes, G.L., Kubie, J.L., and Muller, R.U. (2009). Recurrent seizures induce a reversible impairment in a spatial hidden goal task. *Hippocampus* 19, 817–827. <https://doi.org/10.1002/hipo.20565>
4. Sass, K.J., Spencer, D.D., Kim, J.H., Westerveld, M., Novelly, R.A., and Lencz, T. (1990). Verbal memory impairment correlates with hippocampal pyramidal cell density. *Neurology* 40, 1694–1697. <https://doi.org/10.1212/wnl.40.11.1694>
5. Zhao, F., Kang, H., You, L., Rastogi, P., Venkatesh, D., and Chandra, M. (2014). Neuropsychological deficits in temporal lobe epilepsy: A comprehensive review. *Ann. Indian Acad. Neurol.* 17, 374–382. <https://doi.org/10.4103/0972-2327.144003>
6. Abrahams, S., Morris, R.G., Polkey, C.E., Jarosz, J.M., Cox, T.C., Graves, M., and Pickering, A. (1999). Hippocampal involvement in spatial and working memory: a structural MRI analysis of patients with unilateral mesial temporal lobe sclerosis. *Brain Cognit.* 41, 39–65. <https://doi.org/10.1006/brcg.1999.1095>
7. Guerreiro, C.A.M., Jones-Gotman, M., Andermann, F., Bastos, A., and Cendes, F. (2001). Severe Amnesia in Epilepsy: Causes, Anatomopsychological Considerations, and Treatment. *Epilepsy Behav.* 2, 224–246. <https://doi.org/10.1006/ebeh.2001.0167>
8. Ploner, C.J., Gaymard, B.M., Rivaud-Péchoux, S., Baulac, M., Clémenceau, S., Samson, S., and Pierrot-Deseilligny, C. (2000). Lesions affecting the parahippocampal cortex yield spatial memory deficits in humans. *Cerebr. Cortex* 10, 1211–1216. <https://doi.org/10.1093/cercor/10.12.1211>
9. Celiker Uslu, S., Yuksel, B., Tekin, B., Sarıahmetoglu, H., and Atakli, D. (2019). Cognitive impairment and drug responsiveness in mesial temporal lobe epilepsy. *Epilepsy Behav.* 90, 162–167. <https://doi.org/10.1016/j.yebeh.2018.10.034>
10. Chan, A.Y., Rolston, J.D., Rao, V.R., and Chang, E.F. (2018). Effect of neurostimulation on cognition and mood in refractory epilepsy. *Epilepsia Open* 3, 18–29. <https://doi.org/10.1002/epi4.12100>
11. Beesley, S., Sullenberger, T., Crotty, K., Ailani, R., D'orio, C., Evans, K., Ogunkunle, E.O., Roper, M.G., and Kumar, S.S. (2020). D-serine mitigates cell loss associated with temporal lobe epilepsy. *Nat. Commun.* 11, 4966. <https://doi.org/10.1038/s41467-020-18757-2>
12. Blümcke, I., Thom, M., Aronica, E., Armstrong, D.D., Bartolomei, F., Bernasconi, A., Bernasconi, N., Bien, C.G., Cendes, F., Coras, R., et al. (2013). International consensus classification of hippocampal sclerosis in temporal lobe epilepsy: a Task Force report from the ILAE Commission on Diagnostic Methods. *Epilepsia* 54, 1315–1329. <https://doi.org/10.1111/epi.12220>
13. Swartz, B.E., Houser, C.R., Tomiyasu, U., Walsh, G.O., DeSalles, A., Rich, J.R., and Delgado-Escueta, A. (2006). Hippocampal cell loss in posttraumatic human epilepsy. *Epilepsia* 47, 1373–1382. <https://doi.org/10.1111/j.1528-1167.2006.00602.x>
14. You, J., Huang, H., Chan, C.T.Y., and Li, L. (2021). Pathological Targets for Treating Temporal Lobe Epilepsy: Discoveries From Microscale to Macroscale. *Front. Neurol.* 12, 779558. <https://doi.org/10.3389/fneur.2021.779558>
15. Peng, Z., Zhang, N., Wei, W., Huang, C.S., Cetina, Y., Otis, T.S., and Houser, C.R. (2013). A reorganized GABAergic circuit in a model of epilepsy: evidence from optogenetic labeling and stimulation of somato-statin interneurons. *J. Neurosci.* 33, 14392–14405. <https://doi.org/10.1523/JNEUROSCI.2045-13.2013>
16. Tauck, D.L., and Nadler, J.V. (1985). Evidence of functional mossy fiber sprouting in hippocampal formation of kainic acid-treated rats. *J. Neurosci.* 5, 1016–1022. <https://doi.org/10.1523/JNEUROSCI.05-04-01016.1985>

17. Zhang, W., Yamawaki, R., Wen, X., Uhl, J., Diaz, J., Prince, D.A., and Buckmaster, P.S. (2009). Surviving hilar somatostatin interneurons enlarge, sprout axons, and form new synapses with granule cells in a mouse model of temporal lobe epilepsy. *J. Neurosci.* 29, 14247–14256. <https://doi.org/10.1523/JNEUROSCI.3842-09>.
18. Christenson Wick, Z., Leintz, C.H., Xamonthiene, C., Huang, B.H., and Krook-Magnuson, E. (2017). Axonal sprouting in commissurally projecting parvalbumin-expressing interneurons. *J. Neurosci. Res.* 95, 2336–2344. <https://doi.org/10.1002/jnr.24011>.
19. Lévesque, M., Avoli, M., and Bernard, C. (2016). Animal models of temporal lobe epilepsy following systemic chemoconvulsant administration. *J. Neurosci. Methods* 260, 45–52. <https://doi.org/10.1016/j.jneumeth.2015.03.009>.
20. Téllez-Zenteno, J.F., and Hernandez-Ronquillo, L. (2012). A review of the epidemiology of temporal lobe epilepsy. *Epilepsy Res Treat.* 2012, 630853. <https://doi.org/10.1155/2012/630853>.
21. Tramoni-Negre, E., Lambert, I., Bartolomei, F., and Felician, O. (2017). Long-term memory deficits in temporal lobe epilepsy. *Rev. Neurol.* 173, 490–497. <https://doi.org/10.1016/j.neurol.2017.06.011>.
22. Pierre-Pascal Lenck-Santini, L.M.d.I.P. (2022). *Neurobiology of the Epilepsies: From Epilepsy: A Comprehensive Textbook* (Lippincott Williams & Wilkins).
23. Begus, K., and Bonawitz, E. (2020). The rhythm of learning: Theta oscillations as an index of active learning in infancy. *Dev. Cogn. Neurosci.* 45, 100810. <https://doi.org/10.1016/j.dcn.2020.100810>.
24. Kaplan, R., Doeller, C.F., Barnes, G.R., Litvak, V., Düzel, E., Bandettini, P.A., and Burgess, N. (2012). Movement-related theta rhythm in humans: coordinating self-directed hippocampal learning. *PLoS Biol.* 10, e1001267. <https://doi.org/10.1371/journal.pbio.1001267>.
25. Korotkova, T., Ponomarenko, A., Monaghan, C.K., Poulet, S.L., Cacucci, F., Wills, T., Hasselmo, M.E., and Lever, C. (2018). Reconciling the different faces of hippocampal theta: The role of theta oscillations in cognitive, emotional and innate behaviors. *Neurosci. Biobehav. Rev.* 85, 65–80. <https://doi.org/10.1016/j.neubiorev.2017.09.004>.
26. Buzsáki, G., and Moser, E.I. (2013). Memory, navigation and theta rhythm in the hippocampal-entorhinal system. *Nat. Neurosci.* 16, 130–138. <https://doi.org/10.1038/nn.3304>.
27. Mysin, I., and Shubina, L. (2022). From mechanisms to functions: The role of theta and gamma coherence in the intrahippocampal circuits. *Hippocampus* 32, 342–358. <https://doi.org/10.1002/hipo.23410>.
28. Fries, P. (2005). A mechanism for cognitive dynamics: neuronal communication through neuronal coherence. *Trends Cognit. Sci.* 9, 474–480. <https://doi.org/10.1016/j.tics.2005.08.011>.
29. Myers, J.C., Chinn, L.K., Sur, S., and Golob, E.J. (2021). Widespread theta coherence during spatial cognitive control. *Neuropsychologia* 160, 107979. <https://doi.org/10.1016/j.neuropsychologia.2021.107979>.
30. Jacobs, J., Kahana, M.J., Ekstrom, A.D., and Fried, I. (2007). Brain oscillations control timing of single-neuron activity in humans. *J. Neurosci.* 27, 3839–3844. <https://doi.org/10.1523/JNEUROSCI.4636-06.2007>.
31. Stewart, M., Quirk, G.J., Barry, M., and Fox, S.E. (1992). Firing relations of medial entorhinal neurons to the hippocampal theta rhythm in urethane anesthetized and walking rats. *Exp. Brain Res.* 90, 21–28. <https://doi.org/10.1007/BF00229252>.
32. Newman, E.L., and Hasselmo, M.E. (2014). Grid cell firing properties vary as a function of theta phase locking preferences in the rat medial entorhinal cortex. *Front. Syst. Neurosci.* 8, 193. <https://doi.org/10.3389/fnsys.2014.00193>.
33. Mizuseki, K., Sirota, A., Pastalkova, E., and Buzsáki, G. (2009). Theta oscillations provide temporal windows for local circuit computation in the entorhinal-hippocampal loop. *Neuron* 64, 267–280. <https://doi.org/10.1016/j.neuron.2009.08.037>.
34. Rutishauser, U., Ross, I.B., Mamelak, A.N., and Schuman, E.M. (2010). Human memory strength is predicted by theta-frequency phase-locking of single neurons. *Nature* 464, 903–907. <https://doi.org/10.1038/nature08860>.
35. Shuman, T., Aharoni, D., Cai, D.J., Lee, C.R., Chavlis, S., Page-Harley, L., Vetere, L.M., Feng, Y., Yang, C.Y., Mollinedo-Gajate, I., et al. (2020). Breakdown of spatial coding and interneuron synchronization in epileptic mice. *Nat. Neurosci.* 23, 229–238. <https://doi.org/10.1038/s41593-019-0559-0>.
36. Lenck-Santini, P.P., and Holmes, G.L. (2008). Altered phase precession and compression of temporal sequences by place cells in epileptic rats. *J. Neurosci.* 28, 5053–5062. <https://doi.org/10.1523/JNEUROSCI.5024-07.2008>.
37. Liu, X., Muller, R.U., Huang, L.T., Kubie, J.L., Rotenberg, A., Rivard, B., Cilio, M.R., and Holmes, G.L. (2003). Seizure-induced changes in place cell physiology: relationship to spatial memory. *J. Neurosci.* 23, 11505–11515. <https://doi.org/10.1523/JNEUROSCI.23-37-11505.2003>.
38. Ewell, L.A., Fischer, K.B., Leibold, C., Leutgeb, S., and Leutgeb, J.K. (2019). The impact of pathological high-frequency oscillations on hippocampal network activity in rats with chronic epilepsy. *Elife* 8, e42148. <https://doi.org/10.7554/elife.42148>.
39. Chauvière, L., Rafrati, N., Thinus-Blanc, C., Bartolomei, F., Esclapez, M., and Bernard, C. (2009). Early deficits in spatial memory and theta rhythm in experimental temporal lobe epilepsy. *J. Neurosci.* 29, 5402–5410. <https://doi.org/10.1523/JNEUROSCI.4699-08.2009>.
40. Pasquetti, M.V., Meier, L., Marafiga, J.R., Barbieri Caus, L., Tort, A.B.L., and Calcagnotto, M.E. (2019). Hippocampal CA1 and cortical interictal oscillations in the pilocarpine model of epilepsy. *Brain Res.* 1722, 146351. <https://doi.org/10.1016/j.brainres.2019.146351>.
41. Laurent, F., Brotons-Mas, J.R., Cid, E., Lopez-Pigozzi, D., Valero, M., Gal, B., and de la Prida, L.M. (2015). Proximodistal structure of theta coordination in the dorsal hippocampus of epileptic rats. *J. Neurosci.* 35, 4760–4775. <https://doi.org/10.1523/JNEUROSCI.4297-14.2015>.
42. Lencz, T., McCarthy, G., Bronen, R.A., Scott, T.M., Inserrni, J.A., Sass, K.J., Novelty, R.A., Kim, J.H., and Spencer, D.D. (1992). Quantitative magnetic resonance imaging in temporal lobe epilepsy: relationship to neuropathology and neuropsychological function. *Ann. Neurol.* 31, 629–637. <https://doi.org/10.1002/ana.410310610>.
43. Du, F., Whetsell, W.O., Jr., Abou-Khalil, B., Blumenkopf, B., Lothman, E.W., and Schwarcz, R. (1993). Preferential neuronal loss in layer III of the entorhinal cortex in patients with temporal lobe epilepsy. *Epilepsy Res.* 16, 223–233.
44. Jutila, L., Ylinen, A., Partanen, K., Alafuzoff, I., Mervaala, E., Partanen, J., Vapalahti, M., Vainio, P., and Pitkänen, A. (2001). MR volumetry of the entorhinal, perirhinal, and temporopolar cortices in drug-refractory temporal lobe epilepsy. *AJNR. Am. J. Neuroradiol.* 22, 1490–1501.
45. Bonilha, L., Kobayashi, E., Rorden, C., Cendes, F., and Li, L.M. (2003). Medial temporal lobe atrophy in patients with refractory temporal lobe epilepsy. *J. Neurol. Neurosurg. Psychiatry* 74, 1627–1630. <https://doi.org/10.1136/jnnp.74.12.1627>.
46. Vismer, M.S., Forcelli, P.A., Skopin, M.D., Gale, K., and Koubeissi, M.Z. (2015). The piriform, perirhinal, and entorhinal cortex in seizure generation. *Front. Neural Circ.* 9, 27. <https://doi.org/10.3389/fncir.2015.00027>.
47. Clifford, D.B., Olney, J.W., Maniotis, A., Collins, R.C., and Zorumski, C.F. (1987). The functional anatomy and pathology of lithium-pilocarpine and high-dose pilocarpine seizures. *Neuroscience* 23, 953–968. [https://doi.org/10.1016/0306-4522\(87\)90171-0](https://doi.org/10.1016/0306-4522(87)90171-0).
48. Howard, L.R., Javadi, A.H., Yu, Y., Mill, R.D., Morrison, L.C., Knight, R., Loftus, M.M., Staskute, L., and Spiers, H.J. (2014). The hippocampus and entorhinal cortex encode the path and Euclidean distances to goals during navigation. *Curr. Biol.* 24, 1331–1340. <https://doi.org/10.1016/j.cub.2014.05.001>.
49. Kanter, B.R., Lykken, C.M., Avesar, D., Weible, A., Dickinson, J., Dunn, B., Borgesius, N.Z., Roudi, Y., and Kentros, C.G. (2017). A Novel Mechanism for the Grid-to-Place Cell Transformation Revealed by Transgenic

- Depolarization of Medial Entorhinal Cortex Layer II. *Neuron* 93, 1480–1492.e6. <https://doi.org/10.1016/j.neuron.2017.03.001>.
50. Hafting, T., Fyhn, M., Molden, S., Moser, M.B., and Moser, E.I. (2005). Microstructure of a spatial map in the entorhinal cortex. *Nature* 436, 801–806. <https://doi.org/10.1038/nature03721>.
  51. Solstad, T., Boccara, C.N., Kropff, E., Moser, M.B., and Moser, E.I. (2008). Representation of geometric borders in the entorhinal cortex. *Science* 322, 1865–1868. <https://doi.org/10.1126/science.1166466>.
  52. Sargolini, F., Fyhn, M., Hafting, T., McNaughton, B.L., Witter, M.P., Moser, M.B., and Moser, E.I. (2006). Conjunctive representation of position, direction, and velocity in entorhinal cortex. *Science* 312, 758–762. <https://doi.org/10.1126/science.1125572>.
  53. Kropff, E., Carmichael, J.E., Moser, M.B., and Moser, E.I. (2015). Speed cells in the medial entorhinal cortex. *Nature* 523, 419–424. <https://doi.org/10.1038/nature14622>.
  54. Basu, J., and Siegelbaum, S.A. (2015). The Corticohippocampal Circuit, Synaptic Plasticity, and Memory. *Cold Spring Harbor Perspect. Biol.* 7, a021733. <https://doi.org/10.1101/cshperspect.a021733>.
  55. Canto, C.B., Wouterlood, F.G., and Witter, M.P. (2008). What does the anatomical organization of the entorhinal cortex tell us? *Neural Plast.* 2008, 381243. <https://doi.org/10.1155/2008/381243>.
  56. Mircheva, Y., Peralta, M.R., and Tóth, K. (2019). Interplay of Entorhinal Input and Local Inhibitory Network in the Hippocampus at the Origin of Slow Inhibition in Granule Cells. *J. Neurosci.* 39, 6399–6413. <https://doi.org/10.1523/JNEUROSCI.2976-18.2019>.
  57. Leroy, F., Brann, D.H., Meira, T., and Siegelbaum, S.A. (2019). Input-Timing-Dependent Plasticity in the Hippocampal CA2 Region and Its Potential Role in Social Memory. *Neuron* 102, 260–262. <https://doi.org/10.1016/j.neuron.2019.03.021>.
  58. Froriep, U.P., Kumar, A., Cosandier-Rimélé, D., Häussler, U., Kilias, A., Haas, C.A., and Egert, U. (2012). Altered theta coupling between medial entorhinal cortex and dentate gyrus in temporal lobe epilepsy. *Epilepsia* 53, 1937–1947. <https://doi.org/10.1111/j.1528-1167.2012.03662.x>.
  59. Leite, J.P., Nakamura, E.M., Lemos, T., Masur, J., and Cavalheiro, E.A. (1990). Learning impairment in chronic epileptic rats following pilocarpine-induced status epilepticus. *Trials* 23, 681–683.
  60. Detour, J., Schroeder, H., Desor, D., and Nehlig, A. (2005). A 5-month period of epilepsy impairs spatial memory, decreases anxiety, but spares object recognition in the lithium-pilocarpine model in adult rats. *Epilepsia* 46, 499–508. <https://doi.org/10.1111/j.0013-9580.2005.38704.x>.
  61. Kalemenev, S.V., Zubareva, O.E., Frolova, E.V., Sizov, V.V., Lavrentyeva, V.V., Lukomskaya, N.Y., Kim, K.K., Zaitsev, A.V., and Magazanik, L.G. (2015). Impairment of exploratory behavior and spatial memory in adolescent rats in lithium-pilocarpine model of temporal lobe epilepsy. *Dokl. Biol. Sci.* 463, 175–177. <https://doi.org/10.1134/S0012496615040055>.
  62. Gröticke, I., Hoffmann, K., and Loscher, W. (2007). Behavioral alterations in the pilocarpine model of temporal lobe epilepsy in mice. *Exp. Neurol.* 207, 329–349. <https://doi.org/10.1016/j.expneurol.2007.06.021>.
  63. Murai, T., Okuda, S., Tanaka, T., and Ohta, H. (2007). Characteristics of object location memory in mice: Behavioral and pharmacological studies. *Physiol. Behav.* 90, 116–124. <https://doi.org/10.1016/j.physbeh.2006.09.013>.
  64. Vogel-Ciernia, A., and Wood, M.A. (2014). Examining object location and object recognition memory in mice. *Curr. Protoc. Neurosci.* 69, 8.31.1–8.31.17. <https://doi.org/10.1002/0471142301.ns0831s69>.
  65. Mumby, D.G., Gaskin, S., Glenn, M.J., Schramek, T.E., and Lehmann, H. (2002). Hippocampal damage and exploratory preferences in rats: memory for objects, places, and contexts. *Learn. Mem.* 9, 49–57. <https://doi.org/10.1101/lm.41302>.
  66. Tenant, S.A., Fischer, L., Garden, D.L.F., Gerlei, K.Z., Martinez-Gonzalez, C., McClure, C., Wood, E.R., and Nolan, M.F. (2018). Stellate Cells in the Medial Entorhinal Cortex Are Required for Spatial Learning. *Cell Rep.* 22, 1313–1324. <https://doi.org/10.1016/j.celrep.2018.01.005>.
  67. Du, F., Eid, T., Lothman, E.W., Köhler, C., and Schwarcz, R. (1995). Preferential neuronal loss in layer III of the medial entorhinal cortex in rat models of temporal lobe epilepsy. *J. Neurosci.* 15, 6301–6313. <https://doi.org/10.1523/JNEUROSCI.15-10-06301.1995>.
  68. Fujikawa, D.G. (1996). The temporal evolution of neuronal damage from pilocarpine-induced status epilepticus. *Brain Res.* 725, 11–22. [https://doi.org/10.1016/0006-8993\(96\)00203-x](https://doi.org/10.1016/0006-8993(96)00203-x).
  69. Wozny, C., Gabriel, S., Jandova, K., Schulze, K., Heinemann, U., and Behr, J. (2005). Entorhinal cortex entrains epileptiform activity in CA1 in pilocarpine-treated rats. *Neurobiol. Dis.* 19, 451–460. <https://doi.org/10.1016/j.nbd.2005.01.016>.
  70. Biagini, G., Baldelli, E., Longo, D., Contrini, M.B., Guerrini, U., Sironi, L., Gelosa, P., Zini, I., Ragsdale, D.S., and Avoli, M. (2008). Proepileptic influence of a focal vascular lesion affecting entorhinal cortex-CA3 connections after status epilepticus. *J. Neuropathol. Exp. Neurol.* 67, 687–701. <https://doi.org/10.1097/NEN.0b013e318181b8ae>.
  71. Wang, L., Liu, Y.H., Huang, Y.G., and Chen, L.W. (2008). Time-course of neuronal death in the mouse pilocarpine model of chronic epilepsy using Fluoro-Jade C staining. *Brain Res.* 1241, 157–167. <https://doi.org/10.1016/j.brainres.2008.07.097>.
  72. Scholl, E.A., Dudek, F.E., and Ekstrand, J.J. (2013). Neuronal degeneration is observed in multiple regions outside the hippocampus after lithium pilocarpine-induced status epilepticus in the immature rat. *Neuroscience* 252, 45–59. <https://doi.org/10.1016/j.neuroscience.2013.07.045>.
  73. Dudek, F.E. (2020). Loss of GABAergic Interneurons in Seizure-Induced Epileptogenesis—Two Decades Later and in a More Complex World. *Epilepsy Curr.* 20, 70S–72S. <https://doi.org/10.1177/1535759720960464>.
  74. Dinocourt, C., Petanjek, Z., Freund, T.F., Ben-Ari, Y., and Esclapez, M. (2003). Loss of interneurons innervating pyramidal cell dendrites and axon initial segments in the CA1 region of the hippocampus following pilocarpine-induced seizures. *J. Comp. Neurol.* 459, 407–425. <https://doi.org/10.1002/cne.10622>.
  75. Ikenari, T., Kurata, H., Satoh, T., Hata, Y., and Mori, T. (2020). Evaluation of Fluoro-Jade C Staining: Specificity and Application to Damaged Immature Neuronal Cells in the Normal and Injured Mouse Brain. *Neuroscience* 425, 146–156. <https://doi.org/10.1016/j.neuroscience.2019.11.029>.
  76. Gusel'nikova, V.V., and Korzhevskiy, D.E. (2015). NeuN As a Neuronal Nuclear Antigen and Neuron Differentiation Marker. *Acta Naturae* 7, 42–47.
  77. Siegel, M., Donner, T.H., and Engel, A.K. (2012). Spectral fingerprints of large-scale neuronal interactions. *Nat. Rev. Neurosci.* 13, 121–134. <https://doi.org/10.1038/nrn3137>.
  78. Buzsáki, G., Anastassiou, C.A., and Koch, C. (2012). The origin of extra-cellular fields and currents—EEG, ECoG, LFP and spikes. *Nat. Rev. Neurosci.* 13, 407–420. <https://doi.org/10.1038/nrn3241>.
  79. Navas-Olive, A., Valero, M., Jurado-Parras, T., de Salas-Quiroga, A., Averkin, R.G., Gambino, G., Cid, E., and de la Prida, L.M. (2020). Multi-modal determinants of phase-locked dynamics across deep-superficial hippocampal sublayers during theta oscillations. *Nat. Commun.* 11, 2217. <https://doi.org/10.1038/s41467-020-15840-6>.
  80. Valero, M., Navas-Olive, A., de la Prida, L.M., and Buzsáki, G. (2022). Inhibitory conductance controls place field dynamics in the hippocampus. *Cell Rep.* 40, 111232. <https://doi.org/10.1016/j.celrep.2022.111232>.
  81. Zutshi, I., Valero, M., Fernandez-Ruiz, A., and Buzsaki, G. (2022). Extrinsic control and intrinsic computation in the hippocampal CA1 circuit. *Neuron* 110, 658–673. <https://doi.org/10.1016/j.neuron.2021.11.015>.
  82. Ouchi, A., and Fujisawa, S. (2024). Predictive grid coding in the medial entorhinal cortex. *Science* 385, 776–784. <https://doi.org/10.1126/science.adc4166>.

83. González, J., Cavelli, M., Mondino, A., Rubido, N., Bl Tort, A., and Torterolo, P. (2020). Communication Through Coherence by Means of Cross-frequency Coupling. *Neuroscience* 449, 157–164. <https://doi.org/10.1016/j.neuroscience.2020.09.019>.
84. Hummel, F., and Gerloff, C. (2005). Larger interregional synchrony is associated with greater behavioral success in a complex sensory integration task in humans. *Cerebr. Cortex* 15, 670–678. <https://doi.org/10.1093/cercor/bhh170>.
85. Brandt, C., and Mula, M. (2016). Anxiety disorders in people with epilepsy. *Epilepsy Behav.* 59, 87–91. <https://doi.org/10.1016/j.yebeh.2016.03.020>.
86. Fan, L.Z., Kim, D.K., Jennings, J.H., Tian, H., Wang, P.Y., Ramakrishnan, C., Randles, S., Sun, Y., Thadhani, E., Kim, Y.S., et al. (2023). All-optical physiology resolves a synaptic basis for behavioral timescale plasticity. *Cell* 186, 543–559.e19. <https://doi.org/10.1016/j.cell.2022.12.035>.
87. Bittner, K.C., Milstein, A.D., Grienberger, C., Romani, S., and Magee, J.C. (2017). Behavioral time scale synaptic plasticity underlies CA1 place fields. *Science* 357, 1033–1036. <https://doi.org/10.1126/science.aan3846>.
88. Bittner, K.C., Grienberger, C., Vaidya, S.P., Milstein, A.D., Macklin, J.J., Suh, J., Tonegawa, S., and Magee, J.C. (2015). Conjunctive input processing drives feature selectivity in hippocampal CA1 neurons. *Nat. Neurosci.* 18, 1133–1142. <https://doi.org/10.1038/nn.4062>.
89. Grienberger, C., and Magee, J.C. (2022). Entorhinal cortex directs learning-related changes in CA1 representations. *Nature* 611, 554–562. <https://doi.org/10.1038/s41586-022-05378-6>.
90. Matteo Guardamagna, O.C., Stella, F., Zhang, Q., Kentros, C., and Battaglia, F.P. (2023). Direct Entorhinal Control of CA1 Temporal Coding. Preprint at bioRxiv. <https://doi.org/10.1101/2023.05.27.542579>.
91. Kumar, S.S., and Buckmaster, P.S. (2006). Hyperexcitability, interneurons, and loss of GABAergic synapses in entorhinal cortex in a model of temporal lobe epilepsy. *J. Neurosci.* 26, 4613–4623. <https://doi.org/10.1523/JNEUROSCI.0064-06.2006>.
92. Kumar, S.S., Jin, X., Buckmaster, P.S., and Huguenard, J.R. (2007). Recurrent circuits in layer II of medial entorhinal cortex in a model of temporal lobe epilepsy. *J. Neurosci.* 27, 1239–1246. <https://doi.org/10.1523/JNEUROSCI.3182-06.2007>.
93. Kobayashi, M., Wen, X., and Buckmaster, P.S. (2003). Reduced inhibition and increased output of layer II neurons in the medial entorhinal cortex in a model of temporal lobe epilepsy. *J. Neurosci.* 23, 8471–8479. <https://doi.org/10.1523/JNEUROSCI.23-24-08471.2003>.
94. Feng, Y., and Shuman, T. (2022). Blame it on the Inputs: Overexcited Entorhinal Inputs Drive Dentate Gyrus Hyperexcitability in a Mouse Model of Dravet Syndrome. *Epilepsy Curr.* 22, 372–374. <https://doi.org/10.1177/15357597221112801>.
95. Mattis, J., Somarowthu, A., Goff, K.M., Jiang, E., Yom, J., Sotuyo, N., McGarry, L.M., Feng, H., Kaneko, K., and Goldberg, E.M. (2022). Cortico-hippocampal circuit dysfunction in a mouse model of Dravet syndrome. *eLife* 11, e69293. <https://doi.org/10.7554/eLife.69293>.
96. Wick, Z.C., Philipsberg, P.A., Lamsifer, S.I., Kohler, C., Katanov, E., Feng, Y., Humphrey, C., and Shuman, T. (2023). Manipulating single-unit theta phase-locking with PhaSER: An open-source tool for real-time phase estimation and manipulation. Preprint at bioRxiv. <https://doi.org/10.1101/2023.02.21.529420>.
97. Lo, M.C., Younk, R., and Widge, A.S. (2020). Paired Electrical Pulse Trains for Controlling Connectivity in Emotion-Related Brain Circuitry. *IEEE Trans. Neural Syst. Rehabil. Eng.* 28, 2721–2730. <https://doi.org/10.1109/TNSRE.2020.3030714>.
98. Neves, L., Lobão-Soares, B., Araujo, A.P.d.C., Furtunato, A.M.B., Paiva, I., Souza, N., Morais, A.K., Nascimento, G., Gavioli, E., Tort, A.B.L., et al. (2022). Theta and gamma oscillations in the rat hippocampus support the discrimination of object displacement in a recognition memory task. *Front. Behav. Neurosci.* 16, 970083. <https://doi.org/10.3389/fnbeh.2022.970083>.
99. Philipsberg, P.A., Christenson Wick, Z., Diego, K.S., Vaughan, N., Galas, A., Jurkowski, A., Feng, Y., Vetere, L.M., Chen, L., Soler, I., et al. (2023). Chronotate: An open-source tool for manual timestamping and quantification of animal behavior. *Neurosci. Lett.* 814, 137461. <https://doi.org/10.1016/j.neulet.2023.137461>.
100. Cai, D.J., Aharoni, D., Shuman, T., Shobe, J., Biane, J., Song, W., Wei, B., Veshkini, M., La-Vu, M., Lou, J., et al. (2016). A shared neural ensemble links distinct contextual memories encoded close in time. *Nature* 534, 115–118. <https://doi.org/10.1038/nature17955>.
101. Aronov, D., and Tank, D.W. (2014). Engagement of neural circuits underlying 2D spatial navigation in a rodent virtual reality system. *Neuron* 84, 442–456. <https://doi.org/10.1016/j.neuron.2014.08.042>.
102. Shobe, J.L., Claar, L.D., Parhami, S., Bakurin, K.I., and Masmanidis, S.C. (2015). Brain activity mapping at multiple scales with silicon microprobes containing 1,024 electrodes. *J. Neurophysiol.* 114, 2043–2052. <https://doi.org/10.1152/jn.00464.2015>.
103. Schomburg, E.W., Fernández-Ruiz, A., Mizuseki, K., Berényi, A., Anastassiou, C.A., Koch, C., and Buzsáki, G. (2014). Theta phase segregation of input-specific gamma patterns in entorhinal-hippocampal networks. *Neuron* 84, 470–485. <https://doi.org/10.1016/j.neuron.2014.08.051>.
104. Chrobak, J.J., and Buzsáki, G. (1998). Gamma oscillations in the entorhinal cortex of the freely behaving rat. *J. Neurosci.* 18, 388–398. <https://doi.org/10.1523/JNEUROSCI.18-01-00388.1998>.
105. Lubenov, E.V., and Siapas, A.G. (2009). Hippocampal theta oscillations are travelling waves. *Nature* 459, 534–539. <https://doi.org/10.1038/nature08010>.
106. Karlsson, K.A.E., and Blumberg, M.S. (2004). Temperature-induced reciprocal activation of hippocampal field activity. *J. Neurophysiol.* 91, 583–588. <https://doi.org/10.1152/jn.00953.2003>.
107. Hafting, T., Fyhn, M., Bonnevie, T., Moser, M.B., and Moser, E.I. (2008). Hippocampus-independent phase precession in entorhinal grid cells. *Nature* 453, 1248–1252. <https://doi.org/10.1038/nature06957>.
108. George Paxinos, K.B.J.F. (2019). *Paxinos and Franklin's the Mouse Brain in Stereotaxic Coordinates* (Academic press).
109. Bokil, H., Andrews, P., Kulkarni, J.E., Mehta, S., and Mitra, P.P. (2010). Chronux: a platform for analyzing neural signals. *J. Neurosci. Methods* 192, 146–151. <https://doi.org/10.1016/j.jneumeth.2010.06.020>.
110. Partha, P., and Mitra, H.B. (2008). *Observed Brain Dynamics*.
111. Vanderwolf, C.H. (1969). Hippocampal electrical activity and voluntary movement in the rat. *Electroencephalogr. Clin. Neurophysiol.* 26, 407–418. [https://doi.org/10.1016/0013-4694\(69\)90092-3](https://doi.org/10.1016/0013-4694(69)90092-3).
112. McFarland, W.L., Teitelbaum, H., and Hedges, E.K. (1975). Relationship between hippocampal theta activity and running speed in the rat. *J. Comp. Physiol. Psychol.* 88, 324.
113. Steinmetz, N.A., Aydin, C., Lebedeva, A., Okun, M., Pachitariu, M., Bauza, M., Beau, M., Bhagat, J., Böhm, C., Broux, M., et al. (2021). Neuropixels 2.0: A miniaturized high-density probe for stable, long-term brain recordings. *Science* 372, eabf4588. <https://doi.org/10.1126/science.abf4588>.
114. Pachitariu, M., Sridhar, S., and Stringer, C. (2023). Solving the spike sorting problem with Kilosort. Preprint at bioRxiv. <https://doi.org/10.1101/2023.01.07.523036>.
115. Girish, V., and Vijayalakshmi, A. (2004). Affordable image analysis using NIH Image/ImageJ. *Indian J. Cancer* 41, 47.
116. Schneider, C.A., Rasband, W.S., and Eliceiri, K.W. (2012). NIH Image to ImageJ: 25 years of image analysis. *Nat. Methods* 9, 671–675. <https://doi.org/10.1038/nmeth.2089>.
117. Berens, P. (2009). *CircStat: a MATLAB toolbox for circular statistics*. *J. Stat. Software* 31.

## STAR★METHODS

### KEY RESOURCES TABLE

REAGENT or RESOURCE	SOURCE	IDENTIFIER
<b>Antibodies</b>		
Rabbit anti-NeuN	Millipore Sigma	Cat# AB78N; RRID: AB_10807945
FluoroJade C	Biosensis	Cat# TR-100-FJ
Alexa Goat Anti-Rabbit 555	Thermo Fisher Scientific	Cat# A21429; RRID:AB_2535850
Alexa Goat Anti-Rabbit 488	Thermo Fisher Scientific	Cat# A11008; RRID:AB_143165
<b>Chemicals, peptides, and recombinant proteins</b>		
Pilocarpine Hydrochloride	Sigma-Aldrich	Cat# P6503; CAS# 54-71-7
Scopolamine Methyl Nitrate	Sigma-Aldrich	Cat# S2250; CAS# 155-41-9
Diazepam	DASH Pharmaceuticals	NDC# 69339-137-01
DPX	Thermo Fisher Scientific	Cat# 50980369
Histo Clear II (Xylene)	Thermo Fisher Scientific	Cat# 5032947
DAPI	Thermo Fisher Scientific	Cat# D1306
Trypsin	gibco	Cat# 15090-046
Dil Dye	Invitrogen	Cat# V22885
Isoflurane	Baxter Healthcare Corporation	NDC# 10019-360-40
Paraformaldehyde	Wako	Cat# 163-20145
HEPES	Sigma-Aldrich	Cat# V900477
NaCl	Sigma-Aldrich	Cat# V900058
KCl	Sigma-Aldrich	Cat# V900068
CaCl <sub>2</sub>	Sigma-Aldrich	Cat# V900269
MgCl <sub>2</sub>	Sigma-Aldrich	Cat# V900020
Triton X-100	Thermo Fisher Scientific, Fisher BioReagents	Cat# BP151-100; CAS# 9002-93-1
Normal Goat Serum	Calbiochem	Cat# NS02L
phosphate buffered saline (PBS)	Thermo Fisher Scientific	Cat# bp339-500
Carprofen	Rimadyl (Through Mount Sinai Pharmacy)	Cat# 4019449
Lidocaine (Xylocaine 2%)	Premier ProRX (Through Mount Sinai Pharmacy)	Cat# PRX480627
Ampicillin	Sigma Aldrich	Cat# A0166-5G
<b>Deposited data</b>		
Original code	This paper	<a href="https://doi.org/10.5281/zenodo.14341007">https://doi.org/10.5281/zenodo.14341007</a>
Raw LFP and extracted spike data	This paper; DANDI Archive	<a href="https://dandiarchive.org">https://dandiarchive.org</a> , dataset #000638
<b>Experimental models: Organisms/strains</b>		
Mouse: C56BL/6	Charles River	Strain# 027
Mouse: 129X1/SvJ (OVX mice)	Jackson Lab	Strain# 000691; RRID:IMSR_JAX:000691
<b>Software and algorithms</b>		
MATLAB	The Mathworks, Inc	<a href="https://www.mathworks.com/">https://www.mathworks.com/</a>
Python	Open-source	<a href="https://www.python.org/">https://www.python.org/</a>
Prism 9.3	GraphPad Software Inc	<a href="https://www.graphpad.com/updates/prism-931-release-notes">https://www.graphpad.com/updates/prism-931-release-notes</a>
NeuroScore	DSI	Version 3.3.9318
Biorender	Biorender	<a href="https://www.biorender.com/">https://www.biorender.com/</a>
ImageJ	NIH	<a href="https://imagej.net/Fiji">https://imagej.net/Fiji</a>
Adobe Illustrator	Adobe	N/A
Miniscope recording software	Open-source	<a href="https://github.com/Aharoni-Lab/Miniscope-DAQ-QT-Software">https://github.com/Aharoni-Lab/Miniscope-DAQ-QT-Software</a>
Chronotate	Open-source; Philipsberg et al. <sup>99</sup>	<a href="https://github.com/ShumanLab/Chronotate">https://github.com/ShumanLab/Chronotate</a>
Cell counter	Open-source	<a href="https://github.com/ZachPenn/CellCounting">https://github.com/ZachPenn/CellCounting</a>

## EXPERIMENTAL MODEL AND STUDY PARTICIPANT DETAILS

### Study design

All experimental procedures were approved by the Icahn School of Medicine's Institutional Animal Care and Use Committee (IACUC), in accordance with the US National Institutes of Health (NIH) guidelines. For EEG recordings, we used wireless EEG devices from Data Science International (DSI) to continuously monitor seizure activity prior to silicon probe recordings. For silicon probe acute recordings, we used two 256-channel probes from UCLA Masmanidis Lab to simultaneously record in HPC and MEC at 3 or 8 weeks after pilocarpine-induced status epilepticus (Pilo-SE).

### Animals

Adult male C57BL/6 mice (Charles Rivers Laboratories) were used in all experiments. Male mice had lower mortality rates in preliminary studies and were previously utilized to identify changes in the progression of spatial coding deficits after Pilo-SE.<sup>35</sup> We therefore restricted our sample to only male mice in this study. Outside of water restriction, mice were given *ad libitum* food and water on a 12-h light-dark cycle. Mice were group housed with 4–5 per cage until wireless EEG recording started. Mice were then separated into individual housing for recording purposes and co-housed with one ovariectomized female mouse (129X1/SvJ, The Jackson Laboratory). Pilocarpine-induced status epilepticus occurred at 9 weeks of age.

## METHOD DETAILS

### Wireless EEG and headbar implant surgical procedures

3–4 weeks before *in vivo* electrophysiology recordings, all mice underwent headbar and wireless EEG implantation surgeries. During the surgery, animals were head fixed on the surgical stereotax (KOPF Instruments) and maintained under anesthesia with 1–3% isoflurane (Baxter Healthcare Corporation, NDC 10019-360-40). The scalp was cleared of hair and sterilized with betadine (Purdue Frederick, NDC 0034-2200-80) and 70% ethanol. Once the skull was exposed, the fascia was cleared with 3% hydrogen peroxide (MEDLINE, NDC: 53329-981-06). The animal's skull was then aligned to the stereotax using bregma and lambda. To implant the EEG device (Data Science International, model ETA-F10), we enlarged the scalp opening to the neck area and used blunt, bent forceps to open the cavity under the back skin. We then inserted the body of the EEG device into the back underneath the back skin, with two lead wires exposed from the neck area. Two burr holes were then made on different hemispheres. 1mm length of insulation was stripped off from the tip of both wire leads before inserting into the burr hole and securing between the dura and skull with cyanoacrylate glue. To allow for head-fixation during recordings, we secured a stainless steel headbar to the skull using glue and dental cement (LANG Dental Mfg, ref. 1330, ref. 1306), and then built up the dental cement to create a well around the exposed skull. Kwik-Sil (World Precision Instruments, Cat# 600022) was then used to fill the well. A final layer of cement was then applied on top of the Kwik-Sil and the headbar. Lidocaine (Premier ProRX, Cat# PRX480627, 2%, ~0.05mL) was injected subcutaneously into the neck area to assist with recovery from EEG implantation. In addition, carprofen (Rimadyl, Cat# 4019449, 5 mg/kg) was administered during surgery and for 2 days after and ampicillin (Sigma Aldrich, Cat# A0166-5G, 20 mg/kg) was administered during surgery and for 6 additional days.

### Pilocarpine-induced status epilepticus

Mice were randomly assigned to receive either saline or pilocarpine injections at 9 weeks of age. On the day of injection, all animals first received a 0.1 mL intraperitoneal injection of scopolamine methyl bromide (0.2 mg/mL, Sigma-Aldrich, Cat# P6503; CAS# 54-71-7) to reduce the peripheral effects of pilocarpine. 30 min later, all pilocarpine-assigned mice received intraperitoneal injections of pilocarpine hydrochloride (Sigma-Aldrich, Cat# S2250; CAS# 155-41-9), with the dose depending on their body weight (250 mg/kg if more than 25 g; 275 mg/mL if between 20 and 25 g; 285 mg/kg if less than 20 g). Saline-assigned mice received equivalent volumes of saline (Fresenius Medical Care, Cat# 060-10109) instead. If pilocarpine-treated mice had not seized within 45 min of the initial pilocarpine injection, booster injections of 50–100 mg/kg pilocarpine were given. Status epilepticus (SE) was established when animals entered a continuous seizure, and didn't react to outside stimuli. Pilocarpine-treated mice were left in SE for 2 h, after which they received a 20 mg/kg intraperitoneal injection of diazepam (DASH Pharmaceuticals, NDC 69339-137-01) to terminate SE. Pilocarpine-treated mice who didn't reach SE or died during the procedure were excluded from the study (SE success rate ~75%). All other animals were given 1 mL of saline through subcutaneous injection by the end of the day, access to moistened food, and were monitored for 72 h to ensure recovery. Additional saline was given if pilocarpine-treated animals were slow to recover. Wireless EEG transmitters were turned on after SE induction in mice recorded 3 weeks after Pilo-SE. For mice recorded 8 weeks after Pilo-SE, EEGs were turned on 5 weeks after Pilo-SE. In all pilocarpine-treated mice, we confirmed spontaneous seizures through EEG recording.

### Novel object location task

The novel object location task was performed either 3 weeks or 8 weeks after Pilo-SE in both Epileptic and age-matched Control groups. All animals were first habituated to the behavior room for 6 days prior to the test. After being left in the behavior room in their home cage for 20 min, mice were handled by the experimenter for 3 min each day. Animals were then put in an empty box (1 ft × 1 ft) with different wall patterns on each side for 10 min for box habituation on day 7. On the day of the NOL test (day 8), animals were first

put into the empty box to explore without objects for 6 min. We then took them out, cleaned the box with 70% ethanol, and taped down two identical objects (1.5 inches × 2 inches shiny gold door stoppers) at the two corners of the box. Animals were put back in the box for two 6-min training sessions of object exploration (for the Hard version), and this 6-min object exploration period was repeated a third time for the Easy version of the task. The mice were then returned to their home cages for 3-h before the test session. During the test session, one of the two objects was moved to a novel location, and the animals were allowed to explore the box for 6 min. Animals were not pre-exposed to the objects until the training sessions, and they were introduced to the box with objects in a controlled manner by being put in the center of the box with equal distances to both objects. Extra-field spatial cues were consistent throughout the NOL training and testing, with dim overhead lights over each behavior box and a central environmental fan providing white noises. Animals were transferred from the vivarium to the behavior room on a cart in a controlled and consistent way, with black light-blocking cloth covering all cages. All sessions were recorded with webcams using the v3 Miniscope recording software<sup>35,100</sup> (available at <https://github.com/Aharoni-Lab/Miniscope-DAQ-QT-Software>) to record multiple videos simultaneously. Training and test recordings were then scored by a technician who was blinded to the experimental group. Investigation times and durations were recorded using Chronotate<sup>99</sup> (available at <https://github.com/ShumanLab/Chronotate>). The animal's preference to investigate either object was indicated by a discrimination index (DI):

$$\text{DI} = \frac{\text{Interaction time with moved object} - \text{Interaction time with unmoved object}}{\text{Total interaction time}} \times 100$$

A higher DI during the test means a stronger preference for the moved object, indicating intact spatial memory of the unmoved object. Note that animals with |DI| higher than 30 during training, explored either object for less than 3 s during training, or spent a total less than 3 s exploring objects during testing were excluded from the analysis ( $N = 1$  excluded from 3wk Easy Task;  $N = 0$  excluded from 8wk Easy Task;  $N = 6$  excluded from 3wk Hard Task;  $N = 1$  excluded from 8wk Hard Task).

### **Virtual reality (VR) training**

Mice were trained to navigate a virtual linear track to obtain water rewards. As such, they were water restricted during training starting from initial handling. Mice had access to 1-2mL of water daily to maintain their body weight around 85% of their initial weight, which was measured right before water deprivation started.<sup>35</sup> More water was offered immediately if mice showed any sign of dehydration or if their body weight was below 78%. Training began with 2 days of handling followed by 2 days of handling plus habituation to head-fixation. Next, mice were introduced to the Styrofoam ball and were given 3 days to habituate to walking on the ball while head-fixed. Then we added lick training, during which animals were trained to lick at a metal tube for water while head-fixed on the ball. Virtual reality (VR) linear track training started after animals could reliably gain water from the lick port. Our VR setup included three 24-inch flat monitor screens (DELL) that angled 120° to each other and surrounded the animal. ViRMEn<sup>101</sup> (available at <http://pni.princeton.edu/pni-software-tools/virmen>), an open-source MATLAB software, was used to create the virtual environment. Animals were trained to run down VR tracks of increasing length to release a 5uL water drop at the end of the VR track. Mice were considered ready for silicon probe recording when they could reach at least 100 trials within 1 h on the longest track (2m in the real world). The VR training phase typically lasted 5–7 days.

### **Craniotomy and ground implantation surgery**

Craniotomy and ground wire implantation happened the day prior to acute silicon probe recording. Animals were lightly anesthetized with isoflurane and head-fixed on the stereotax. The top layer of cement was drilled off, and Kwik-Sil was removed to expose the skull. A burr hole was then made over the cerebellum, on the left side. The ground wire (Ag/AgCl-coated, Warner Instruments) was slipped into the burr hole to sit above the dura. A small drop of cyanoacrylate glue was used to secure the ground wire in place. 1.6mm wide craniotomy was then made above HPC (centered at 2mm posterior to bregma, 1.8mm right of bregma) and MEC (centered at 250um anterior to the superior cerebellar artery; 3.3mm right of bregma). The craniotomies were covered with buffered artificial cerebrospinal fluid<sup>35,100</sup> (ACSF; in mM: 135 NaCl, 5KCl, 5 HEPES, 2.4 CaCl<sub>2</sub>, 2.1 MgCl<sub>2</sub>, pH 7.4) and Kwik-Sil was then applied to the skull to cover and protect the craniotomies. Animal received a carprofen (Rimadyl, Cat# 4019449, 5 mg/kg) injection after the craniotomy to reduce pain and prevent inflammation.

### **Acute silicon probe recordings**

On the day of recording, we first painted the 256-channel probes (UCLA Masmanidis lab, HPC probe: 4 shanks, 400 μm apart; MEC shank: 4 shanks, 200 μm apart) with Dil (Invitrogen, Vybrant Dil, V22885) to be able to visualize and check the probe tract after recording.<sup>102</sup> Mice first received carprofen (Rimadyl, Cat# 4019449, 5 mg/kg) before being head-fixed onto the Styrofoam ball. We removed the Kwik-Sil and replaced it with buffered ACSF.<sup>35,100</sup> The mouse's skull was then aligned to the micromanipulator (ROE-200, Sutter Instrument) and the ground wire was connected to the air table ground. We then attached the two 256-channel probes to a micromanipulator and lowered them into HPC (coordinates for middle shank: 1.95mm posterior, 1.65mm right, and 2.3mm ventral from bregma) and MEC (coordinates for middle shank: 190um anterior to the superior cerebellar artery, and 3.05mm right, and 3.3mm ventral to bregma) slowly at ~5um/s. We used a custom MATLAB script to plot raw and filtered data, the theta phase shift, and coherence for each region. We used these electrophysiological features to determine if the probes

were in the correct location.<sup>33,103–107</sup> Once probes were both in place, we applied mineral oil (Fisher Chemical, Cat# 8042-47-5) over the buffered ACSF and the brain was allowed to settle for 1 h.

During recording, each probe was connected to two 128-channel headstages (Intan Technologies, Cat# C3316) to organize and amplify the signals. Signals were recorded with an Intan recording controller (Intan Technologies, INTAN 1024ch Recording Controller) to collect and log electrophysiology signals from each channel at 25kHz. Licking behavior, reward delivery times, animals' position on the virtual track, and running speed were logged through the Intan I/O Expander connected to the Intan Recording Controller at the same sampling rate of 25kHz and were saved on a local computer through Intan RHX Data Acquisition Software.

Animals were allowed to run in the 2m long VR track to earn water rewards at least 100 times. Then we switched the animal into a novel environment and allowed another ~100 trials in the novel context. The average total recording length was ~180 min. Note that all data presented here was taken while animals were traversing the VR track they had been previously trained on (i.e., was familiar).

### Histology confirmation of probe track

Following the recording, we removed the probes from the animal's brain and rinsed them with MilliQ water before putting them in 2.5% trypsin (gibco, Cat# 15090-046) for 40 min. The mouse was deeply anesthetized using 4% isoflurane before performing a quick decapitation. The brain was extracted and put in 4% paraformaldehyde (PFA; Wako, Cat# 163-20145) and kept at 4°C for 24 h before changing into fresh phosphate buffered saline (1xPBS; Thermo Fisher Scientific, Cat# bp339-500). The right hemisphere of the brain was sectioned sagittally using the vibratome (Leica VT1000S) at 80 µm. Sections were then stained for NeuN and DAPI to help differentiate MEC layers (see Immunohistochemistry). Three excitation wavelengths were used to capture the probe tracts and anatomical structures (Dil, wavelength 555), DAPI (wavelength 408), and NeuN staining (wavelength 488). For each shank, we referenced the mouse brain atlas<sup>108</sup> to validate the probe location. Only shanks that were in the correct HPC and MEC locations covering all or partial sublayers (CA1-DG layers for HPC; MEC layer 1–3 for MEC) were included in the analysis. Example shanks can be found in Figure S3.

### Post-processing and analysis of local field potential data

All data analysis was performed in custom MATLAB and Python scripts. We first took the minute-by-minute raw data and concatenated it into continuous signals for each channel.

For local field potential (LFP) analysis, all data were first down-sampled to 1kHz. We cleaned out 60Hz noise by passing a custom notch filter in MATLAB. Data were then filtered by different bandpass filters with a focus on theta (5–12 Hz) oscillations. Theta phase shift and coherence were then measured using the Chronux toolbox.<sup>109,110</sup> Using electrophysiology features (theta peak power,<sup>105</sup> theta/gamma phase shift,<sup>33,104,105</sup> theta/gamma coherence,<sup>103,107</sup> dentate spike phase reversal,<sup>106</sup> spike density) and probe tract histology images, we were able to identify the location of each channel within the sublayers of HPC and MEC. The power plot (Figure 3A) was generated by averaging theta power for each subregion. Because seizures and locomotion are known to impact theta power,<sup>111,112</sup> we limited our analyses to periods when the animal was locomoting and not seizing (the mouse needed to be moving continuously for more than 3 s to be considered locomoting; once a seizure was detected, the seizing period and the 10min after the seizure were excluded from analysis).

Coherence analyses were performed using the Chronux toolbox.<sup>109,110</sup> Each channel pair generated a theta coherence value. To do group analysis, a uniform-shaped sub-region matrix was generated for each animal, and the coherence value for a given region-pair was assigned to the sub-region matrix for group comparison analysis. Coherence data were exported from MATLAB and plotted in Python for visualization (Figures 3B, 6A, and 6B). To perform the coherence subsampling analysis (Figures 7 and S10), recordings were broken into 1-s bins. Then cross region MEC-HPC (MEC2 to DG molecular layer) coherence, within region HPC (DG hilus to CA1 pyramidal layer) coherence, and within region MEC (MEC2 to MEC3 molecular layer) coherence were calculated for each bin. To determine when Epileptic animals' theta coherence values were similar to Controls, we selected the time bins in 3-week and 8-week Epileptic animals that showed theta coherence within 0.5 standard deviations of the Control group's coherence value (Figure S10A), which last at least for 2 s. Cross-region and within-region coherences were then recalculated within these subsample of time bins (Figures 7 and S10) to study the relationship between coherence deficits of different region pairs. Note that all subsample analyses were done during periods of locomotion.

The proportion of within- and cross-region subsampled bins across the track (Figure S10D) was calculated using a subsample occupancy map. We first calculated the spatial occupancy of the animals. We restricted the analysis to periods of locomotion and down-sampled the data temporally by 10x, resulting in an effective sampling rate of 2.5kHz. We then divided the track into 30 spatial bins (approximately 6.6cm wide), and the spatial occupancy of the animals was calculated as the number of samples in each spatial bin divided by the effective sampling rate. In other words, the spatial occupancy of the animals is the time (in seconds) the animal spent in each spatial bin. To obtain the occupancy map for each subsample (i.e., HPC-MEC, HPC, MEC), we further restricted our analysis to include only the samples that occurred within each subsampled time. We then calculated the spatial occupancy for each subsample in the same way as the per-animal spatial occupancy, resulting in the number of seconds the animal spent in each spatial bin restricted to the subsampled time bins. We then divided this subsampled occupancy map by the per-animal occupancy map independently for each spatial bin. The result was between 0 and 1 element-wise (for each spatial bin), and can be interpreted as the proportion of time the animal spent during the subsampled time in a spatial bin relative to the total time the animal

spent in a given spatial bin. Finally, we normalized the occupancy map for each subsample independently so that the sum of the proportions equals 1, allowing easier comparison when the total time for each subsampled analysis differs across different subsample criteria.

Note that animals were excluded from all subsampled plots if insufficient time bins were available to create a subsampled dataset with coherence equivalent to Controls.

### Single unit spike sorting and phase preference analysis

To extract single unit activity, the raw electrophysiological data from each shank was first background subtracted in a custom MATLAB script. Background subtracted data were then passed into kilosort 2.5, an automatic spike sorting package using a template-matching approach with drift correction.<sup>113,114</sup> Phy2<sup>113</sup> was used to manually confirm and clean each unit as needed. All single unit analyses were carried out in MATLAB using custom scripts.

Spike-sorted units were first classified as putative inhibitory and excitatory units in HPC and MEC based on their firing rate, waveform characteristics, and autocorrelogram.<sup>33,35,81</sup> In HPC, units with a firing rate below 8Hz, complex spike index over zero, mean autocorrelogram less than 0.1, and c index (trough-to-peak latency) above 0.26 were classified as excitatory cells. Units with firing rates over 0.2Hz and mean autocorrelogram greater than 0.1 were classified as inhibitory cells (Figure S7A). In MEC, we performed kmeans clustering based on c index (trough-to-peak latency) to separate inhibitory and excitatory units<sup>33</sup> (Figure S7B).

We quantified phase preference to local or downstream theta oscillation by measuring the mean phase of firing (mu value) and phase locking strength (R value) of each cell. Note that only cells with significant r-values (i.e., were significantly phase-locked; Rayleigh's test for non-uniformity) were included in the phase preference (mu) analysis (see [quantification and statistical analysis](#)). To isolate reference theta for phase preference analysis, the raw data were filtered to the bandwidth of interest (5-12Hz), and a representative channel was picked for each region as reference oscillation (middle channel in MEC2/3 as local MEC theta; middle channel in hilus as DG theta; top channel in pyramidal cell layer as CA1 theta). The theta phase angle was then determined using the Hilbert transformation. MEC3 excitatory cells were separated into trough and peak-locked cells using k-means clustering. Two parameters, R value and mu value, were used during the clustering (Figure 5A). The number of cells per animal is listed in the table titled Cells recorded per animal in Control, 3-week Epileptic, and 8-week Epileptic groups.

**Cells recorded per animal in Control, 3-week Epileptic, and 8-week Epileptic groups.**

	Control	3wk epileptic	8wk epileptic
DG inhibitory cells	17, 20, 13, 13, 24, 32, 22, 28, 25, 15, 4	4, 22, 7, 6, 21, 25, 10, 14, 6, 5	3, 20, 26, 10, 26, 31, 1, 8
MEC2 excitatory cells	12, 10, 3, 14, 33, 14, 18, 11, 69, 14, 16	2, 15, 6, 15, 11, 6, 29, 37, 18, 36	1, 28, 10, 16, 31, 15, 11, 71, 5
MEC3 excitatory cells	13, 5, 10, 26, 52, 16	69, 15, 13, 1, 16, 8	14, 38, 19, 38, 28
MEC3 trough-locked excitatory cells	10, 1, 3, 4, 16, 16	12, 10, 4, 1, 15, 3	2, 29, 4, 27, 5
MEC3 peak-locked excitatory cells	3, 4, 7, 22, 36	57, 5, 9, 1, 5	12, 9, 15, 11, 23

We further calculated different firing properties of spike-sorted cells, including firing rate, peak amplitude ratio (b/a), trough-to-peak latency (c), autocorrelogram, and burst index (Figures S9A–S9F). Specifically, the burst index is calculated by spike count from 2 to 5ms divided by spike count from 200 to 250ms in the autocorrelogram. A secondary clustering method was applied to separate Trough and Peak-locked cells purely by mu value. Cells with mu values between 90 and 270 degrees of theta are classified as Trough-locked, and cells with mu values below 90° or above 270° are classified as Peak-locked cells (Figure S9G).

### EEG seizure quantification

All EEG seizure detection was performed manually by experimenters who were blinded to the animal group information. Neuroscore (DSI, Version 3.3.9318) was used for EEG signal visualization and seizure detection. EEG seizures were identified by a sharp signal amplitude increase, followed by a 2–10 min quiet period. EEG signals were not collected when animals were in training or receiving a craniotomy.

### Interictal epileptic discharge (IED) quantification

IEDs were detected using a custom MATLAB script with full sampling rate data from silicon probe recordings. A sample channel in the HPC pyramidal layer was chosen for IED detection. To be counted as an IED, the event needed to have more than 1200µV amplitude, a minimum of 0.001 s above 1200µV, and a maximum of 0.004 s to reach the trough after reaching the 1200µV threshold. The minimum time window between two IEDs was 1 s. The correlation analysis between IED frequency and theta power and coherence was carried out only during running.

**Immunohistochemistry at different timepoints**

We used FluoroJade C (FJC) and NeuN staining to characterize cell degeneration and neuron number, respectively. We perfused the animals with 1x PBS (Thermo Fisher Scientific, Cat# bp339-500) and 4% PFA (Wako, Cat#163-20145) at 2 days, 3 weeks, or 8 weeks after status epilepticus. Extracted brains were post-fixed in 4% PFA for 12–24 h before being transferred into a 30% sucrose solution (in 1x PBS). Once the brain sank to the bottom of the sucrose solution (~48 h), we cut the brain down the midline and stored the left and right hemispheres in the –80°C freezer.

For NeuN staining, the right hemispheres were sliced sagittally at 40 $\mu$ m on a cryostat (Leica CM3050S). Sections containing HPC or MEC underwent two 15-min washes in 1 X PBS, followed by 2 h of blocking at room temperature in 0.3% Triton X-100 (Fisher BioReagents, Cat# BP151-100) and 3% normal goat serum (Calbiochem, Cat# NS02L) in 1xPBS (diluted from 10xPBS). Next, slices were incubated in rabbit anti-NeuN (Millipore Sigma, ABN78) primary antibody (1:2000, in blocking solution) at 4°C overnight (~15 h). On the next day, slices underwent three 15-min 1xPBS washes. They were then incubated in secondary antibody in PBS (1:500 goat anti-rabbit polyclonal Alexa Fluor 555, Thermo Fisher Scientific, A21429) for 2 h at room temperature while covered in foil. Slices were washed in 1xPBS three times with DAPI (Thermo Fisher Scientific, D1306, at 1:5000) added during the second wash. All washes and incubations took place on a shaker. We then mounted all slices containing HPC and MEC on Super Plus Microscope Slides (Thermo Fisher, 22-037-246) with ProLong Gold mounting solution (Thermo Fisher Scientific, P36930). Slides were sealed with nail polish before being stored at 4°C.

For FJC staining, the left hemispheres were sliced sagittally at 30 $\mu$ m on a cryostat (Leica CM3050S). Biosensis (Ready-to-Dilute) Fluoro-Jade C staining kit (TR-100-FJ) was used for staining. HPC- and MEC-containing sections were then selected and mounted on slides (Thermo Fisher, 22-037-246) and dried at 60°C on a slide warmer for 1 h to allow good adhesion. Slides were then incubated in a Coplin jar (Thermo Fisher, Polypropylene Coplin Staining Jar, 0181621) with 9 parts of 80% ethanol and 1 part of sodium hydroxide (biosensis Fluoro-Jade C staining kit) for 5 min. Slides were transferred to a jar containing 70% ethanol for 2 min and then into distilled water for 2 min. The endogenous fluorescent background was blocked by incubating in 1 part potassium permanganate (biosensis Fluoro-Jade C staining kit) mixed with 9 parts distilled water for 10 min. Slides were then immersed in the FJC staining solution, which contained 1 part of the FJC solution (biosensis Fluoro-Jade C staining kit) and 9 parts of distilled water, for 10 min in the dark. Three rounds of distilled water rinses were followed to clean the dye from the slices before the slides were dried on a slide warmer at 60°C for 10 min in the dark. Finally, slices were cleared by 3 min of immersion in xylene (Thermo Fisher, Histo-Clear II 5032947) before being mounted using DPX (Thermo Fisher, 50980369).

All images were taken by a Leica DM6B fluorescence microscope (Figure S2). Cell counting was performed using an automatic cell counting pipeline (available at <https://github.com/ZachPenn/CellCounting>) in combination with manual counting with the assistance of ImageJ.<sup>115,116</sup>

**QUANTIFICATION AND STATISTICAL ANALYSIS**

Full details for all statistical tests are reported in Table S1.

All statistics were performed in GraphPad Prism 9.3.1 except for the *p*-value matrices and single-unit phase preference (*mu*; circular data), which were calculated in Python3 and MATLAB (R2021b), respectively.

For the *p*-value matrices, a Welch's t test was used between each channel pair across the group. In Figures 4C and 4D, the threshold for significance (*alpha*) was set to 0.05. In Figures 3B and 6, the *alpha* was set to 0.017 to correct for multiple comparisons among the three groups. Only comparisons with a *p*-value below *alpha* were marked in blue (decrease coherence) or red (increase coherence) in the *p*-value matrices.

The Circular Statistic Toolbox<sup>117</sup> in MATLAB was used to calculate and compare circular data (i.e., *mu*). We performed the circular Kuiper test to compare the distributions of two populations and the circular k-test to test the equality of phase concentration parameters between groups. Only group differences that showed significantly different distributions (Kuiper test) were additionally tested for changes in concentration (circular k-test). The asterisks on Figures 3C, 4A, 5B, and 5E represent the significant changes in concentration. The threshold for significance (*alpha*) was placed at \**p* < 0.017, \*\**p* < 0.003, and \*\*\**p* < 0.0003 to account for multiple comparisons across groups.

All other statistics were performed in GraphPad Prism. All data are presented as mean ± SEM, with *n* representing the number of cells and *N* representing the number of animals. To compare theta power along hippocampal layers between the three experimental groups, the Repeated-measures mixed-effects model followed by Holm-Sidak post hoc correction was used. One-way or two-way ANOVAs followed by Bonferroni's post hoc test were used to statistically compare normally distributed data. LFP power and coherence changes were tested for correlation with seizure frequency and seizure recency using a Pearson test and reported with correlation coefficient R value (Figure S5). All statistical tests with post hoc correction were two-tailed with thresholds of significance set at \**p* < 0.05, \*\**p* < 0.01, and \*\*\**p* < 0.001.